Tectonics

RESEARCH ARTICLE
10.1029/2022TC007487

†Deceased 27 July 2018

Key Points:

- Thermal modeling of apatite fission track and (U-Th)/He zircon data from the Pastos Chicos Basin shows Oligo-Miocene onset of exhumation
- Regional compilation of spatio-temporal deformation at 23°–24°S suggests out-of-sequence deformation related to basement heterogeneities
- Mio-Pliocene U–Pb zircon ages of volcanic ash deposits refine the chronostratigraphy of the Pastos Chicos Basin

Supporting Information:

Supporting Information may be found in the online version of this article.

Correspondence to:

H. Pingel,
heiko.pingel@geo.uni-potsdam.de

Citation:

Pingel, H., Deeken, A., Coutand, I., Alonso, R. N., Riller, U., Sobel, E. R., et al. (2023). Cenozoic exhumation and deformation of the intermontane Pastos Chicos Basin in the southern Central Andes: Implications for the tectonic evolution of the Andean Plateau (Puna) and the Eastern Cordillera between 23° and 24°S, NW Argentina. *Tectonics*, *42*, e2022TC007487. https://doi.org/10.1029/2022TC007487

Received 1 JUL 2022
Accepted 9 JAN 2023

Author Contributions:

Conceptualization: Heiko Pingel, Anke Deeken, Manfred R. Strecker
Formal analysis: Heiko Pingel, Anke Deeken, Isabelle Coutand, John M. Cottle
Funding acquisition: Isabelle Coutand, Manfred R. Strecker

Cenozoic Exhumation and Deformation of the Intermontane Pastos Chicos Basin in the Southern Central Andes: Implications for the Tectonic Evolution of the Andean Plateau (Puna) and the Eastern Cordillera Between 23° and 24°S, NW Argentina

Heiko Pingel[1], Anke Deeken[1,†], Isabelle Coutand[2], Ricardo N. Alonso[3], Ulrich Riller[4], Edward R. Sobel[1], John M. Cottle[5], and Manfred R. Strecker[1]

[1]Institut für Geowissenschaften, Universität Potsdam, Potsdam, Germany, [2]Department of Earth Sciences, Dalhousie University, Halifax, NS, Canada, [3]Facultad de Ciencias Naturales, Universidad Nacional de Salta, Salta, Argentina, [4]Institut für Geologie, Universität Hamburg, Hamburg, Germany, [5]Department of Earth Science, UCSB, Santa Barbara, CA, USA

Abstract The Andean Plateau of north-western Argentina (Puna) at a mean elevation of ca. 4.2 km constitutes the southern continuation of the Altiplano; it is a compressional basin-and-range province comprising fault-bounded, high-elevation mountain ranges and largely internally drained basins with often thick sedimentary and volcaniclastic fill. Growing sedimentological and structural evidence supports the notion that the north-western Argentine Andes between 22° and 26°S developed from an initial extensive broken-foreland system that extended across the present-day eastern Andean flank during the early to middle Eocene. However, compelling evidence of the tectonic history of this region is still missing. Here, we present new apatite fission track and zircon (U–Th)/He thermochronological data and U–Pb zircon ages from intercalated volcanic ash deposits from the Pastos Chicos Basin (23.5°S, 66.5°W) to constrain basin formation and the timing of major crustal deformation in the northern Puna. Inverse thermal modeling of the thermochronological data provides further temporal constraints on the late Cenozoic cooling history of the crust in this region and, by inference, on the timing of upper-crustal shortening, range uplift, and basin formation in the northern sector of the present-day Puna Plateau. Specifically, we argue for plateau-wide distributed deformation in the Eocene between 23° and 24°S, followed by spatially disparate and diachronous deformation (Oligocene to Pliocene).

Plain Language Summary The Argentine Puna Plateau is a mountainous region in the Central Andes of South America. It is the result of the tectonic convergence between the oceanic Nazca Plate and the continental South American Plate. However, the detailed tectonic evolution of this region is yet unknown. We present new thermochronologic data from the Puna Plateau that allow inferences about crustal deformation and mountain range uplift. Combined with previous studies, our results suggest deformation distributed over the entire plateau during the Eocene. Thereafter, local deformation occurred spatially non-systematic, possibly related to zones of weakness in the crust.

1. Introduction

Flat-slab subduction is accompanied by strong coupling of converging lithospheric plates resulting in areally extensive upper-plate deformation (e.g., Dickinson & Snyder, 1978; Jordan et al., 1983). In such geodynamic settings, strain is often accommodated along steeply dipping reverse faults originating from the compressional reactivation of basement anisotropies (e.g., Marshak et al., 2000), which may result in a basin-and-range morphology with spatially disparate, diachronous basement uplifts, major changes in fluvial networks and the formation of intervening sedimentary basins. Exemplary regions for this style of deformation are the late Cenozoic Argentine Sierras Pampeanas (e.g., Jordan & Allmendinger, 1986), the Cretaceous-Paleogene Laramide uplifts of North America (e.g., Davis et al., 2009; Ernst, 2010; Marshak et al., 2000; Talling et al., 1995) and the Cenozoic Tien Shan and Qilian Shan of Central Asia (e.g., Sobel & Dumitru, 1997; Sobel et al., 2003; Tapponnier et al., 1990).

The area of the present-day Altiplano-Puna in the southern Central Andes between 21° and 24°S (Figure 1) is currently situated above a ca. 30°-dipping segment of the subducting Nazca plate; this region is thought to have been located over a subhorizontally subducting slab during the late Oligocene to middle Miocene, comparable

Investigation: Heiko Pingel, Ricardo N. Alonso, Ulrich Riller, Manfred R. Strecker
Resources: Ricardo N. Alonso
Supervision: Edward R. Sobel, Manfred R. Strecker
Validation: Edward R. Sobel
Visualization: Heiko Pingel
Writing – original draft: Heiko Pingel, Anke Deeken
Writing – review & editing: Heiko Pingel, Isabelle Coutand, Ricardo N. Alonso, Ulrich Riller, Edward R. Sobel, John M. Cottle, Manfred R. Strecker

to the modern flat-slab segment of the Nazca Plate between approximately 28° and 33°S (e.g., Coira et al., 1993; Ramos, 1999; Ramos & Folguera, 2009). The episode of shallow subduction was inferred from a general gap in volcanic activity in this area between 26 and 14 Ma (Coira et al., 1993; Kay et al., 1999), between 35 and 20 Ma (Haschke et al., 2002), or alternatively between 18 and 12 Ma (Ramos & Folguera, 2009).

Some authors argue for spatially extensive crustal shortening and broken foreland-basin development in late Oligocene to mid-Miocene time in the arc and retroarc regions of the present-day Puna Plateau between 21° and 24°S, consistent with the expected diachronous orogenic growth typical of flat-slab subduction environments (e.g., Riller et al., 2012; Strecker et al., 2009, 2012). Such a broken-foreland scenario with discrete depocenters was also suggested for the mid-Eocene to Oligocene tectonic development of a ~250-km-wide region of the Andes at 25°S, including areas to the east of the present-day plateau region (del Papa et al., 2013; Hongn et al., 2007, 2010; Montero-López et al., 2021). Alternatively, deformation may have propagated sequentially eastward during the Cenozoic evolution of the southern Central Andes (e.g., DeCelles & Horton, 2003; DeCelles et al., 2011; Henríquez et al., 2022). However, the exact timing of deformation in the southern Central Andes is well studied only to the north of 22°S and south of 24°S (e.g., Anderson et al., 2018; Carrapa et al., 2005, 2006; Coutand et al., 2006; DeCelles & Horton, 2003; Deeken et al., 2006; del Papa et al., 2013; Elger et al., 2005, 2007; Kay et al., 2009; Kraemer et al., 1999; McQuarrie, 2002; McQuarrie et al., 2005; Oncken et al., 2006; Reiners et al., 2015; Strecker et al., 2007; Zapata et al., 2020), whereas comparable data from the intervening northern Puna are still scarce (Deeken et al., 2005; Henríquez et al., 2020, 2022; Lapiana, 2021).

A steady foreland-ward propagation of deformation, typical of thin-skinned foreland fold-and-thrust belts and characterized by an advancing deformation front, is promoted by deep sedimentary basins with mechanically weak layers that are prone to form detachment horizons that drive shortening (e.g., Allmendinger et al., 1983). For example, the Subandean fold-and-thrust belt of the southern Central Andes in Bolivia and north-western Argentina is characterized by detachment surfaces in a thick Cambrian-Carboniferous sedimentary sequence (e.g., Allmendinger & Gubbels, 1996; Echavarria et al., 2003). However, this Paleozoic sequence pinches out south of 22°S and deformation in the fold-and-thrust belt is replaced by isolated basement-cored uplifts in the Santa Bárbara System (Kley & Monaldi, 2002; Mon & Salfity, 1995). In addition, the region of the present-day Puna, Eastern Cordillera, and Santa Bárbara System between 22° and 27°S experienced continental extension in the region of the Salta Rift between the Cretaceous-early Paleogene; this extensional province consisted of several sub-basins surrounding a central horst, the Salta-Jujuy high (e.g., Galliski & Viramonte, 1988; Marquillas et al., 2005; Salfity & Marquillas, 1994). Normal faults of the paleo-rift often follow Paleozoic thrust faults and metamorphic foliations (Hongn et al., 2010; Omarini et al., 1999). Many of these structures were reactivated during Cenozoic shortening of the northern part of the Puna Plateau (e.g., Allmendinger et al., 1983; Grier et al., 1991; Hongn et al., 2010; Kley et al., 2005).

Here, we constrain the onset of crustal deformation and associated range uplift in the northern Puna using apatite fission track and zircon (U–Th)/He thermochronology (AFT and ZHe, respectively) from basement rocks collected in the Pastos Chicos Basin and its bounding ranges in the Jujuy Province of north-western Argentina (ca. 23.5°S, 66.5°W, Figure 1). Thermal modeling of AFT data resolves the cooling, and, by inference, deformation history of the basin-bounding ranges of the Pastos Chicos Basin, revealing a distinct episode of basement deformation during the Oligocene and early Miocene. Combined with published data on regional deformation characteristics, our results provide constraints on the spatio-temporal deformation patterns during the early orogenic processes of Andean evolution that later culminated in the formation of the second largest orogenic plateau on Earth.

2. Geological Setting

The Pastos Chicos Basin is an intermontane basin located on the northern Puna Plateau between 23° and 24°S at ca. 3,800 m asl (Figure 1). It is bordered by the fault-bounded Sierra de Tanque and Sierra de Cobres to the west and east, respectively. Both ranges comprise Cambro-Ordovician metasedimentary rocks (Bahlburg, 1990) intruded by Ordovician granitoids (Bahlburg et al., 2016 and references therein) and have been uplifted along basinward-verging, NNE-striking, reverse faults (Figure 2). The basin strata consist mainly of deformed Mio-Pliocene fluvial and alluvial redbeds, conglomerates, and volcaniclastic rocks that unconformably cover the Paleozoic basement rocks (e.g., Schwab, 1973). Whether the basement was at some point overlain by the regionally widespread Eocene Casa Grande Formation (Fernández et al., 1973) is not clear, but cannot be ruled out, as these strata exist in the adjacent Salina de Olaroz/Cauchari area to the west and potentially in the subsurface

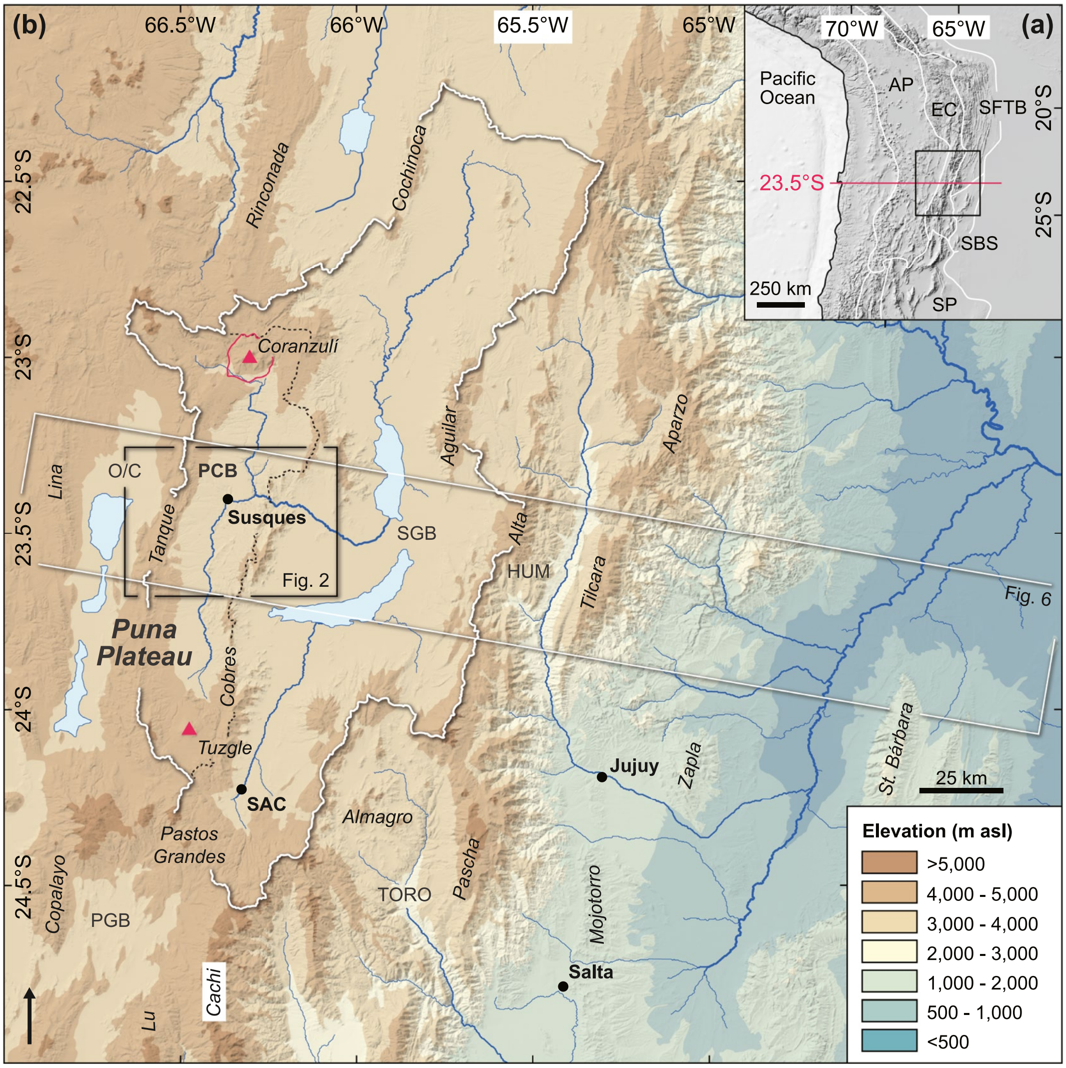

Figure 1. (a) Shaded relief map showing morphotectonic provinces of the Central Andes. Black box shows extent of panel (b). AP—Andean Plateau; EC—Eastern Cordillera; SFTB—Subandean foreland fold-and-thrust belt; SBS—Santa Bárbara System; SP—Sierras Pampeanas. (b) Topographic map of North-western Argentina showing the location of the studied Pastos Chicos Basin (PCB, black frame, Figure 2)—a sub-catchment of the greater Salinas Grandes Basin (white outline) on the northern Puna Plateau. White rectangle delineates area of swath profile shown in Figure 6. Labels in italics represent the names of mountain ranges and volcanoes (red triangle) discussed in the text. PCB—Pastos Chicos; O/C—Olaroz/Cauchari; SGB—Salinas Grandes; PGB—Pastos Grandes; HUM—Humahuaca; and TORO—Toro basins; SAC—San Antonio de los Cobres (town); Lu—Cumbres de Luracatao Range.

of the Salinas Grandes Basin to the east (e.g., Gangui & Götze, 1996; López Steinmetz & Galli, 2015; Seggiaro et al., 2015). The Mio-Pliocene basin deposits consist of the ≥10.8 ± 0.3 Ma Trinchera Formation (henceforth referred to as Upper Vizcachera Formation, following Seggiaro et al., 2015), the ca. 10–4 Ma Pastos Chicos Formation (Schwab, 1973; Schwab & Lippolt, 1976), and a suite of 6.8–6.5 Ma ignimbrites originating from the Cerro Coranzulí volcanic complex to the north (Figure 1; Seggiaro, 1994)—recently discussed in light of a complex, but single, caldera formation at about 6.6 ± 0.2 Ma (Seggiaro et al., 2019).

Today, the Pastos Chicos Basin is drained by the Río de las Burras (fed by the Río Coranzulí and Río Pastos Chicos) through a narrow bedrock gorge east of the town of Susques that routes runoff to the Salinas Grandes Basin. As a result, the basin morphology is characterized by dissected alluvial fans (associated with the Pastos Chicos Formation) and deeply incised canyons (e.g., Schwab, 1973), especially near the town of Susques, while, at the eastern flanks of the Sierra de Cobres in the adjacent Salinas Grandes Basin, the Río de las Burras has formed a ca. 900 km^2 alluvial fan.

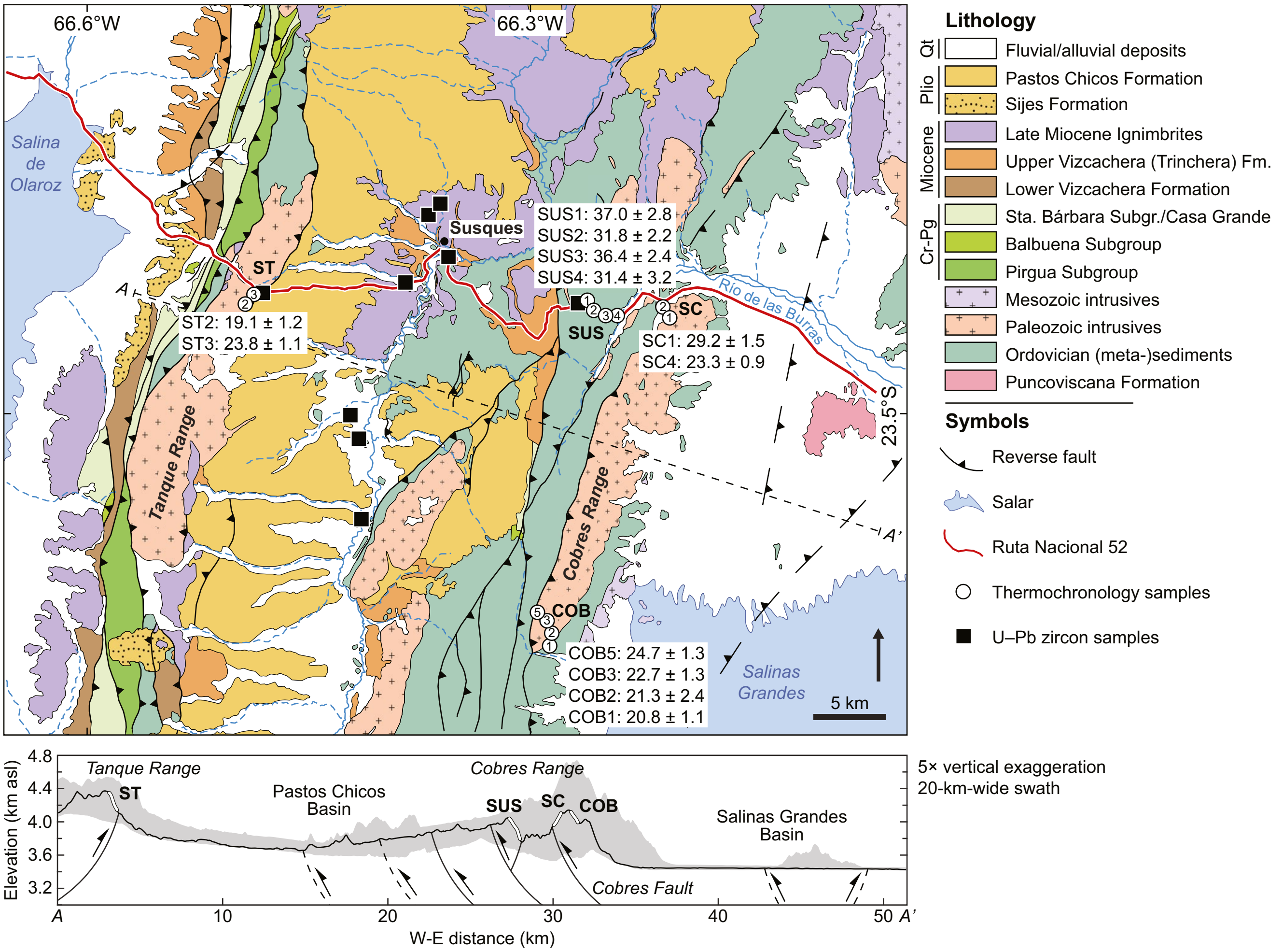

Figure 2. Geological map of the Pastos Chicos Basin (modified from Seggiaro et al. (2015)) showing volcanic ash (squares) and bedrock (numbered circles) sample locations. Numbers denote highest to lowest apatite fission track cooling ages for each vertical transect. The dashed black line (A–A′) marks the centerline of the 20-km-wide topographic swath profile shown below. The profile shows average (black line) and maximum/minimum (gray envelope) elevations, as well as projected sample locations and simplified faults.

The basin-bounding Sierra de Tanque west of the Pastos Chicos Basin comprises a series of bivergent reverse faults placing Ordovician and Cretaceous strata onto the basin deposits, including the Pastos Chicos Formation (e.g., Seggiaro et al., 2015) (Figure 2). South of the town of Susques, outcrops of the Ordovician basement, unconformably overlain by units of the Upper Vizcachera Formation, show several west-verging folds and thrusts (Figure 2, Henríquez et al., 2020). Similar basement outcrops exist within the central part and along the western margin of the Pastos Chicos Basin, indicating that the sedimentary fill is relatively thin. In contrast, the neighboring Olaroz/Cauchari and Salinas Grandes basins to the west and east exhibit ca. 4 km of syn-orogenic sedimentary fill (Coutand et al., 2001; Seggiaro et al., 2015). Linked faults along the center of the Sierra de Cobres (herein referred to as the Cobres Fault) juxtapose rocks of the Cobres Granite (478 ± 4 Ma, Insel et al., 2012) with Paleozoic rocks, and locally Cenozoic strata (Figure 2).

The onset of Cenozoic shortening and mountain building in the northern Puna is recorded by syntectonic strata of the regionally extensive middle Eocene Casa Grande Formation at the eastern Puna Plateau margin (Coutand et al., 2001; Gangui & Götze, 1996; Hongn et al., 2007; Montero-López et al., 2018). This deformation may have affected a ca. 250-km-wide region that is now represented by the present-day Puna Plateau (del Papa et al., 2013; Montero-López et al., 2021). To the west, the Cordillera de Domeyko in northern Chile records rock uplift and rapid exhumation by the middle Eocene to early Oligocene (e.g., Arriagada et al., 2006; Maksaev, 1990; Maksaev & Zentilli, 1999; Mpodozis et al., 2005). Coeval deformation is also documented along the Bolivian proto-Eastern Cordillera (e.g., Benjamin et al., 1987; Ege et al., 2007; Horton et al., 2002; Lamb & Hoke, 1997) and along the present-day eastern Puna Plateau margin in north-western Argentina—for example, the Almagro (ca. 30 Ma from AFT, Andriessen & Reutter, 1994), Nevado de Cachi (ca. 40 Ma from deformed strata, Hongn et al., 2007), Cumbres de Luracatao (≥25 Ma from AFT, Deeken et al., 2006), and Sierra Chango Real ranges (ca. 30 Ma from AFT, Coutand et al., 2001). Late Oligocene deformation is also reported for the Sierra de Rinconada, which constitutes the northern continuation of the Sierra de Tanque, where provenance indicators in the early Oligocene to early Miocene Cabrería Formation (San Juan de Oro Basin) suggest range formation (Caffe & Coira, 2002; López Steinmetz & Montero-López, 2019). Similar observations associated with ranges bordering the Tres Cruces and Casa Grande areas have also been reported (Adelmann, 2001; Insel et al., 2012). Deformation and uplift that lead to the present-day topographic configuration of the adjacent Eastern Cordillera commenced at ca. 15–10 Ma (Deeken et al., 2005; Lapiana, 2021; Pingel et al., 2013, 2014; Siks & Horton, 2011).

3. Methods

3.1. Apatite Fission Track and (U–Th–Sm)/He Zircon Thermochronology

To constrain the cooling history, and by inference, the exhumation and deformation history of mountain ranges bordering the intermontane Pastos Chicos Basin, we collected 12 bedrock samples from four vertical profiles across the Sierra de Tanque and Sierra de Cobres for AFT and selected (U–Th–Sm)/He zircon thermochronology. Two granitic samples from the western basin-bounding Sierra de Tanque (ST profile) were collected from elevations of 4,080 and 4,190 m. Four samples were collected from Ordovician metasedimentary rocks from the western flanks of the Sierra de Cobres (SUS profile) between 3,580 and 3,760 m. Furthermore, samples have been collected from the northern (SC profile) and southern (COB profile) sectors of the Cobres Granite between elevations of 3,580 and 4,280 m. For sample locations see Figure 2 and Table 1.

AFT and (U–Th–Sm)/He zircon (ZHe) thermochronology utilizes the retention of radiogenic decay products below a crystal system- and cooling rate-specific closure temperature to estimate the timing of exhumation and crustal deformation. These closure temperatures represent the base of the partial annealing (PAZ for AFT) and partial retention (PRZ for ZHe) zones. Typically, the temperature range of AFT PAZs is ~120°C to 60°C (e.g., Gleadow & Duddy, 1981) and for ZHe PRZs ~200°C to 130°C (Wolfe & Stockli, 2010), within and above which decay products are not preserved over geological timescales and thermochronological ages are reduced or set to zero.

Bedrock samples were crushed and sieved, and zircons and apatites were extracted by standard magnetic and heavy liquid methods.

AFT analyses used the external detector method (Hurford & Green, 1983); sample preparation followed the procedure outlined by Sobel and Strecker (2003). Apatites were embedded in epoxy, polished, and then etched for 20 s at 21°C with 5.5 N nitric acid. Following irradiation at the Oregon State University TRIGA reactor, muscovite detectors were etched for 45 min at 21°C with 40% hydrofluoric acid. Samples were analyzed with a Leica DMRM microscope at Potsdam University, Germany by A. Deeken (COB and SUS samples) or with a Zeiss Axioskop microscope at Stanford University, U.S.A. by I. Coutand (ST and SC samples). The microscopes were provided with a drawing tube located above a digitizing tablet and a Kinetek computer-controlled stage driven by the FTStage 3.11 program (Dumitru, 1993). Analysis was performed with reflected and transmitted light with 100× air objectives, a 1.25× tube factor, and 10× eyepieces. For age determinations, up to 20 good-quality grains per sample were selected at random and dated. Raw data were reduced using macTrack X software with ζ (for CN5 glass) = 389.9 ± 7.5 and 369.6 ± 5.1 for analysts Anke Deeken and Isabelle Coutand, respectively. Samples with $P(\chi^2) \geq 5\%$ represent a single population (Galbraith & Laslett, 1993; Green, 1981). For such samples, the pooled age is reported, otherwise the central age is reported. To assess the kinetic properties of the apatites, four Dpar measurements (etch-pit length parallel to the c-axis) were averaged from each analyzed crystal (Donelick et al., 1999; Ketcham et al., 1999). The Dpar values of the COB and SUS samples were calibrated using a linear correction factor of 0.87, calculated by comparing Dpar measurements of two age standards (Durango and Fish Canyon Tuff) with those obtained by Donelick et al. (1999) (following Sobel & Seward, 2010). All analytical data can be found in Table 1.

Zircon (U–Th–Sm)/He analyses were carried out on two samples (COB2 and SUS1) at Potsdam University and Helmholtz Centre Potsdam–GFZ German Research Centre for Geosciences using laboratory procedures described in Galetto et al. (2021). Three single grain aliquots were measured per sample. Individual ages were

Table 1
Apatite Fission Track Analytical Data

					Spontaneous		Induced		Dosimeter				Age	Length					Dpar[e]		
Sample	Lithology	Latitude (°S)	Longitude (°W)	Elevation (m)	ρS ($\times 10^6$ cm^{-2})	NS	ρI ($\times 10^6$ cm^{-2})	NI	ρD ($\times 10^6$ cm^{-2})	ND	U (ppm)	P($\chi 2$) (%)	Age $\pm$ 1σ (Ma)	NXL	MTLm (μm)	SD (μm)	MTLc (μm)	SD (μm)	NL	Mean (μm)	SD (μm)
Cobres range																					
COB-5[a]	M	23.626	66.294	4,280	0.5280	480	4.5200	4,109	1.0881	4,678	52.4	95	24.7 ± 1.3	20	12.92	2.45	14.19	1.52	86	1.74[f]	0.08
COB-3[a]	M	23.633	66.287	4,030	0.4440	404	4.1700	3,795	1.0979	4,678	47.5	92	22.7 ± 1.3	20	12.30	2.99	13.97	1.58	39	1.74[f]	0.07
COB-2[a]	M	23.637	66.287	3,860	0.4060	183	4.1300	1,862	1.1078	4,678	46.6	1	21.3 ± 2.4[d]	11	13.15	1.93	14.40	1.28	41	1.71[f]	0.05
COB-1[a]	M	23.639	66.288	3,740	0.5130	485	5.3700	5,070	1.1180	4,678	60.0	99	20.8 ± 1.1	20	12.91	2.18	14.25	1.31	100	1.73[f]	0.07
SC-1[b]	G	23.440	66.210	3,837	0.4296	522	3.1290	3,802	1.1531	6,351	37.0	79	29.2 ± 1.5	20	13.86	1.54	15.06	0.91	13	1.72	0.11
SC-4[b]	MS	23.434	66.215	3,578	0.7390	875	6.7850	8,033	1.1599	6,351	76.0	6	23.3 ± 0.9	15	13.19	1.73	14.50	1.16	21	1.79	0.11
SUS-1[a]	MS	23.427	66.270	3,757	0.2247	228	1.3010	1,320	1.1029	4,459	14.7	96	37.0 ± 2.8	20	12.45	1.81	14.05	1.06	7	1.57[f]	0.09
SUS-2[a]	MS	23.431	66.266	3,748	0.2320	267	1.5600	1,795	1.1098	4,459	17.3	87	31.8 ± 2.2	20	12.01	0.79	13.26	0.20	2	1.58[f]	0.09
SUS-1/2[c]				3,753								97	34.1 ± 1.8	40						1.58[f]	0.09
SUS-3[a]	MS	23.438	66.258	3,682	0.2410	306	1.4390	1,826	1.1168	4,459	15.8	82	36.4 ± 2.4	20	12.37	2.97	13.87	1.99	31	1.48[f]	0.08
SUS-4[a]	MS	23.440	66.247	3,581	0.1030	120	0.7140	835	1.1239	4,459	7.8	100	31.4 ± 3.2	20	12.99	2.72	14.16	1.68	8	1.49[f]	0.06
Tanque range																					
ST-2[b]	G	23.427	66.496	4,190	0.3411	321	3.7150	3,496	1.1260	6,351	46.0	11	19.1 ± 1.2	13	13.53	1.72	14.86	0.96	20	1.58	0.08
ST-3[b]	G	23.426	66.492	4,079	0.6703	664	5.9120	5,856	1.1396	6,351	71.0	7	23.8 ± 1.1	15	13.60	1.74	14.88	1.11	24	1.61	0.09

Note. Lithology: M-Ordovician monzogranite, G-Ordovician granodiorite, MS-Ordovician metasediments of the Complejo de Plataforma de la Puna; ρ_S, ρ_I, ρ_D: density of spontaneous, induced and dosimeter-induced (CN5 glass) tracks, respectively; N_S, N_I, N_D: number of tracks counted to determine the reported track densities (ρ); U: uranium concentration; $P(\chi^2)$: chi-square probability; NXL: number of individual crystals dated; MTLm: mean confined horizontal track length measured; MTLc: C-axis projection of MTLm; NL: numbers of lengths measured; SD: standard deviation.

[a]Analyst A. Deeken (ζ = 389.9 ± 7.5 for CN5 glass). [b]Analyst I. Coutand (ζ = 369.6 ± 5.1 for CN5 glass). [c]Merged data set. [d]Central age, all other ages are pooled ages. [e]Diameter of etch figures parallel to the crystallographic c-axis. [f]Calibrated Dpar values (correction factor: 0.87).

calculated using standard alpha-ejection corrections assuming a homogeneous U and Th distribution (e.g., Farley et al., 1996; Hourigan et al., 2005). Both uncorrected and alpha-ejection corrected cooling ages and additional analytical data are reported in Table S1 in Supporting Information S2.

3.2. Thermal Modeling

Cooling histories were obtained from AFT-length distributions combined with AFT and ZHe ages by inverse modeling using the HeFTy thermal modeling software (version 1.9.3) (Ketcham, 2005).

Time-temperature constraints were set to model a simple cooling path with three constraints (simple cooling models). In cases where ZHe data were available (COB2 and SUS1), the inversion models of all samples from the corresponding profile started within time-temperature conditions of 200°C–300°C, at time intervals well before the obtained ZHe ages. In the case of the SC profile for which no ZHe data were available, we assume starting conditions based on the ZHe data from COB2 and set the initial time-temperature constraint to 160°C–180°C and 75–85 Ma. We consider this to be a viable option to increase the accuracy of the model, as both profiles are from the Sierra de Cobres, whose rocks at this time have probably undergone a similar cooling history. This was not an option for the ST samples. Instead, we chose to set the starting temperature-time constraint between 140°C–200°C and 90–100 Ma, well before the observed AFT ages of 19 and 24 Ma, to allow an unbiased development of time-temperature paths during model runs. Initial model runs identified a relatively broad range of time-temperature histories for all samples but showed clearly defined inflection points associated with distinctive cooling rate variations. To increase the model efficiency, additional model runs were carried out in which the originally identified inflection points were generously enclosed by a second constraint between 60°C and 120°C. The final constraint was set to 15°C ± 5°C at 0 Ma.

To test the hypothesis of burial heating by sedimentary overburden since the middle Eocene, we ran a second set of thermal models (reheating models). During these runs, we applied the same initial T-t conditions as for the simple cooling models, added an additional constraint to “force” an Eocene cooling (25–50 Ma, 30°C–80°C), and altered the following constraints to allow the potential reset of AFT ages (10–25 Ma, 80°C–150°C).

All model constraints are summarized in Table S2 in Supporting Information S2. In general, we ran 30,000 random simulations and derived the oldest tracks and T_As (total annealing temperature at which the oldest track is formed) from the best fitting time-temperature paths. The only exceptions are the simple burial and reburial models of SUS3, where we ran 300,000 random simulations to increase the number of model output results. For the other SUS models, this approach was omitted due to a very small number of track length measurements ($N = 8$ and 9).

3.3. U–Pb Zircon Geochronology

We collected samples of 11 volcanic air-fall deposits from the sedimentary basin fill of the Pastos Chicos Basin for U–Pb zircon dating. Following standard magnetic and heavy liquid mineral separation, zircons were hand-picked, mounted in epoxy, and polished. U, Th, and Pb isotope analysis were obtained using a Laser Ablation Multi-Collector Inductively Coupled Plasma Mass Spectrometer at the University of California, Santa Barbara. The zircon (U–Th)/Pb analytical protocol follows that of Cottle et al. (2013) and Cottle (2014) using standard materials, data reduction, and correction methods described in Wiedenbeck et al. (1995), Andersen (2002), Jackson et al. (2004), Crowley et al. (2007), and Paton et al. (2010). Due to potentially significant pre-eruptive residence times and/or post-eruptive reworking, many of the analyzed samples show a non-uniform pattern of U–Pb zircon age distributions. Therefore, we systematically excluded the oldest ages from our calculations of an average zircon crystallization age until near-unity values for the mean square of weighted deviates (MSWD < 2) were achieved. In addition, we applied a generalized Chauvenet Criterion to the remaining grain ages to identify outliers (Vermeesch, 2018). In those cases where no coherent young population (less than three grains) was found, we infer the youngest $^{206}Pb/^{238}U$ zircon ages to represent a maximum depositional age. All analytical data, instrumental setup, and data on secondary reference zircons can be found in Text S1 in Supporting Information S1 and Tables S3–S5 in Supporting Information S2.

4. Results

4.1. AFT Analytical Results

Bedrock samples from the basin-bounding ranges yielded dominantly late Oligocene to early Miocene AFT cooling ages (Table 1, Figure 3). Ages of the samples from the northern Sierra de Cobres (SC: 23.3 ± 0.9 and 29.2 ± 1.5 Ma) are slightly older than those from the southern Sierra de Cobres (COB: 20.8 ± 1.1 Ma to 24.7 ± 1.3 Ma) and from the Sierra de Tanque (ST: 19.1 ± 1.2 and 23.8 ± 1.1 Ma). In contrast, the four SUS samples, collected between the Cobres and the Susques faults, have late Eocene to early Oligocene AFT ages (31.4 ± 3.2 to 37.0 ± 2.8 Ma).

All ages from the SC and COB profiles are positively correlated with sample elevation, whereas those of the ST samples show no age-elevation relationship (Figure 4). However, the age of sample ST3 (23.8 ± 1.1 Ma) is compatible with those of the COB samples. At first glance, ages of the SUS samples show no clear age-elevation relationship due to an inconsistent age distribution of the topmost samples of the vertical profile (SUS 1 and 2). Because the elevation difference (ca. 10 m) and horizontal separation (less than 600 m) of these samples is relatively small, we combined the AFT data from both samples (Sample SUS-1/2 in Table 1) and thus improved the age-elevation relationship. The apparent exhumation rate derived from the age-elevation relationship of the COB samples is 0.14 ± 0.06 mm/yr between ca. 25 and 21 Ma; 0.04 ± 0.01 mm/yr between ca. 29 and 23 Ma for the SC samples; and 0.09 ± 0.18 mm/yr between ca. 35 and 32 Ma for the SUS samples (Figure 4).

The measured mean track lengths (MTLs) of the SUS1–3 samples and of sample COB3 are short (12.01 ± 0.79 to 12.45 ± 1.81 μm, SD); a characteristic typical of partially annealed samples. In contrast, the MTLs of the remaining samples are relatively long (12.91 ± 2.18 to 13.86 ± 1.54 μm, SD), indicative of faster cooling (Table 1, Figure 3). Also, the fraction of shorter tracks is slightly higher in the SUS samples and in the samples COB3 and COB5. The mean Dpar values (Table 1) of the ST and SUS samples are low (1.48–1.61 μm) compared to those of the remaining samples (1.71–1.79 μm). Low standard deviations of the Dpar values (≤0.11) indicate monokinetic apatite populations in each sample.

Only samples COB1 and COB5 provided a satisfactory number of track-length measurements ($N = 86$ and 100), whereas the number of track-length measurements of the remaining samples ($N \leq 41$) is low compared to the ∼100 counts considered desirable for track-length inversion modeling. The modeled cooling histories of these samples are therefore not well constrained. The cooling histories of the SUS and COB samples are more robust due to additional information from ZHe data.

4.2. ZHe Analytical Results

ZHe analyses were carried out on three single-grain aliquots from two bedrock samples from the Sierra de Cobres. COB2 and SUS1 yielded average weighted, alpha-ejection corrected ZHe ages of 82.5 ± 1.3 Ma (single grain ages: 84.5, 77.3, and 85.7 Ma) and 243.5 ± 3.7 Ma (single grain ages: 244.8, 233.3, and 252.3 Ma), respectively (Table S1 in Supporting Information S2 and Figure 4). Both ages differ significantly from thermal modeling using K-Feldspar $^{40}Ar/^{39}Ar$ thermochronology on the COB1 sample reported by Insel et al. (2012), whose thermal model indicates temperatures of ≥250°C ± 20°C prior to 83 Ma (Figure S1 in Supporting Information S1). Since this approach is controversial (e.g., Popov & Spikings, 2020), we use our new ZHe data to constrain the thermal history of the corresponding samples (COB and SUS series).

4.3. Thermal Modeling Results

4.3.1. Simple Cooling Inversions

The simple-cooling inversions of the COB series yielded oldest track ages that generally increase with sample elevation, from ca. 26–27 Ma at the base to 32 Ma at the top (Table S2 in Supporting Information S2). The modeled T_As range between 100°C and 110°C (Figure 5 and Figure S2 in Supporting Information S1). For samples SC4 and SC1, ages of the oldest tracks are ca. 28 and 32 Ma, respectively; the modeled T_As for both samples are ca. 110°C (Figure 5 and Figure S3 in Supporting Information S1). The inversions of the SUS samples yielded ages of the oldest tracks ranging between 39 and 47 Ma; the modeled T_As are ca. 100°C (Figure 5 and Figure S4 in Supporting Information S1). Finally, the inversions of sample ST3 and ST2 yielded ages of the oldest tracks of 30 and 24 Ma with T_As of ca. 105°C (Figure 5 and Figure S5 in Supporting Information S1).

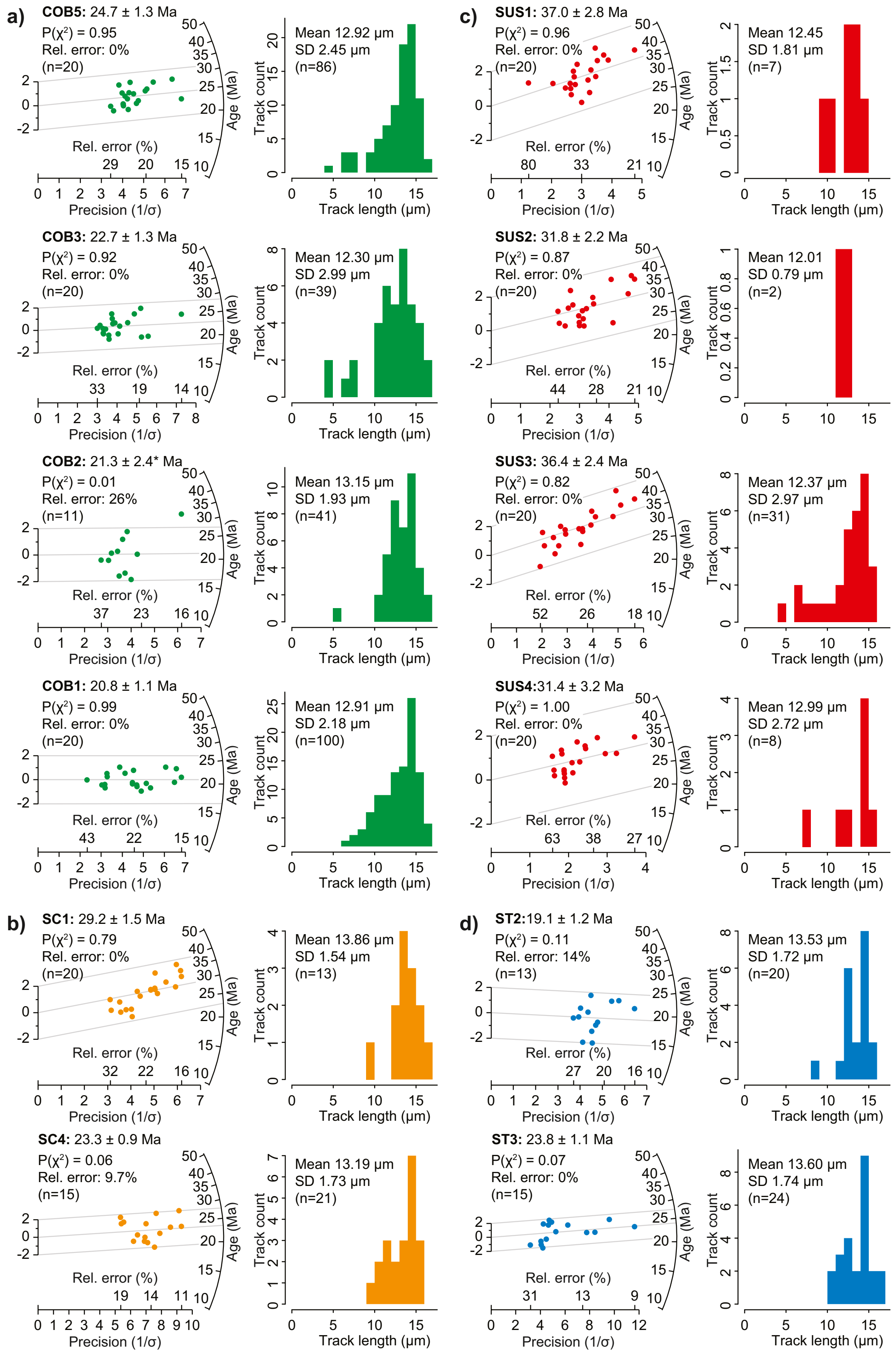
a)
COB5: 24.7 ± 1.3 Ma
P(χ²) = 0.95
Rel. error: 0%
(n=20)
Mean 12.92 μm
SD 2.45 μm
(n=86)
COB3: 22.7 ± 1.3 Ma
P(χ²) = 0.92
Rel. error: 0%
(n=20)
Mean 12.30 μm
SD 2.99 μm
(n=39)
COB2: 21.3 ± 2.4* Ma
P(χ²) = 0.01
Rel. error: 26%
(n=11)
Mean 13.15 μm
SD 1.93 μm
(n=41)
COB1: 20.8 ± 1.1 Ma
P(χ²) = 0.99
Rel. error: 0%
(n=20)
Mean 12.91 μm
SD 2.18 μm
(n=100)
b)
SC1: 29.2 ± 1.5 Ma
P(χ²) = 0.79
Rel. error: 0%
(n=20)
Mean 13.86 μm
SD 1.54 μm
(n=13)
SC4: 23.3 ± 0.9 Ma
P(χ²) = 0.06
Rel. error: 9.7%
(n=15)
Mean 13.19 μm
SD 1.73 μm
(n=21)
c)
SUS1: 37.0 ± 2.8 Ma
P(χ²) = 0.96
Rel. error: 0%
(n=20)
Mean 12.45
SD 1.81 μm
(n=7)
SUS2: 31.8 ± 2.2 Ma
P(χ²) = 0.87
Rel. error: 0%
(n=20)
Mean 12.01
SD 0.79 μm
(n=2)
SUS3: 36.4 ± 2.4 Ma
P(χ²) = 0.82
Rel. error: 0%
(n=20)
Mean 12.37 μm
SD 2.97 μm
(n=31)
SUS4: 31.4 ± 3.2 Ma
P(χ²) = 1.00
Rel. error: 0%
(n=20)
Mean 12.99 μm
SD 2.72 μm
(n=8)
d)
ST2: 19.1 ± 1.2 Ma
P(χ²) = 0.11
Rel. error: 14%
(n=13)
Mean 13.53 μm
SD 1.72 μm
(n=20)
ST3: 23.8 ± 1.1 Ma
P(χ²) = 0.07
Rel. error: 0%
(n=15)
Mean 13.60 μm
SD 1.74 μm
(n=24)
Rel. error (%)
Precision (1/σ)
Age (Ma)
Track count
Track length (μm)

Figure 3.

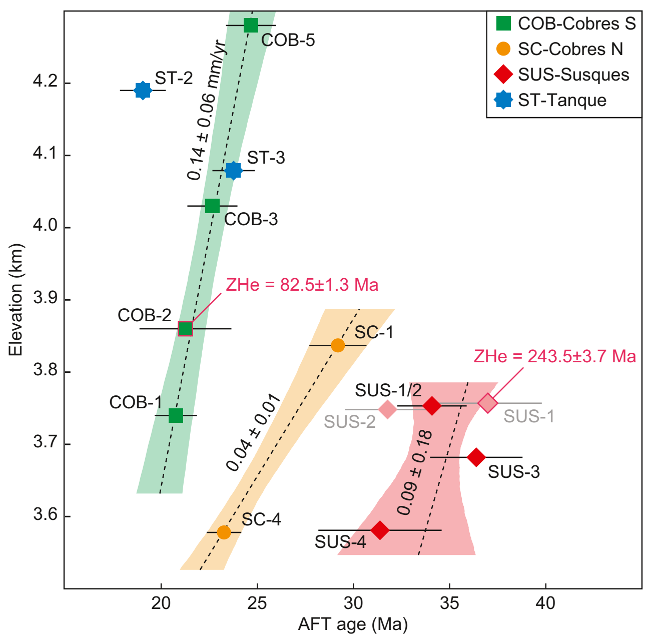

Figure 4. Apatite fission track (AFT) age versus sample elevation. Error bars indicate $\pm 1\sigma$. Dashed lines through AFT ages represent error-weighted linear fit through age-elevation data using a Monte-Carlo approach (Browaeys, 2022); the inverse slope of this line is the apparent exhumation rate (mm/yr).

The COB models suggest rather steady cooling through the ZHe PRZ at ca. 1.3 ± 0.2°C/Ma, followed by an increase of the cooling rates to ca. 3.7 ± 0.3°C/Ma at about 23–20 Ma towards the present surface temperature (unless stated otherwise all cooling rates and their uncertainties represent average and 2 standard deviations calculated from each transects weighted mean paths). The thermal modeling of SC1 and SC4 reveals a similar break in slope (from 1.4 ± 0.2 to 3.2 ± 1.0°C/Ma), but the change in cooling rate appears to occur earlier, between ca. 28 and 22 Ma. Best-fit solutions for SC1 and SC4 suggest that surface temperatures may have been reached by about 20 and 10 Ma, which would require relatively high cooling rates of roughly 9 and 6°C/Ma, respectively. The simple cooling models of the SUS samples all indicate that following an initial, slow cooling of the samples through the ZHe PRZ and AFT PAZ at average cooling rates of ca. 0.3 ± 0.0°C/Ma, samples began rapid cooling. By 33–29 Ma all SUS models exhibit a significant rate change towards rapid cooling until near-surface conditions are attained (on average 2.4 ± 0.3°C/Ma). Both ST models imply rapid cooling since at least 20 Ma (an earlier history is not well constrained) to surface temperatures at an average cooling rate of 3.9 ± 1.4°C/Ma. In both samples, the best-fit model suggest near-surface temperatures by as early as ca. 10 Ma, translating to a cooling rate of approximately 7–8°C/Ma for the rapid cooling phase.

4.3.2. Reheating Inversions

All reheating inversions yielded good statistical results (i.e., good-fit solutions), indicating that burial heating is a possible thermal scenario in the Pastos Chicos Basin. In most cases, however, the calculated oldest tracks (Table S2 in Supporting Information S2, Figure 5 and Figures S2–S5 in Supporting Information S1) postdate the potential reheating history and often even the reheating peak, which renders the pre-oldest track cooling history uninterpretable.

Exceptions are reheating inversions of COB5, SUS3, and SUS4, whose oldest tracks predate an initial cooling and subsequent reheating history. COB5 shows an initial cooling to 60°C between ca. 85 Ma (ZHe) and 41 Ma (3.0°C/Ma), followed by reheating to 108°C by 28 Ma (3.7°C/Ma) and a subsequent cooling to surface temperatures since ca. 28 Ma at rates of 3.3°C/Ma. SUS3 records an initial cooling to 60°C between ca. 245 Ma (ZHe) and 44 Ma (0.5°C/Ma), followed by reheating to 101°C by 30 Ma (2.9°C/Ma) and subsequent cooling to surface temperatures since ca. 30 Ma at rates of 2.9°C/Ma. Results from SUS4 are largely consistent with SUS3. Apart from the onset, the final cooling histories of all reheating-model runs are congruent with the respective simple cooling inversions.

4.4. U–Pb Zircon Results and Chronostratigraphy

Obtained U–Pb zircon ages from tuffs in the Pastos Chicos Basin range between 7.1 and 3.4 Ma and are summarized in Table 2. These ages partly confirm earlier results and help further refine the chronostratigraphy of tectono-sedimentary processes in the Puna. Based on our radiometric data and geological field observations, we are able to clearly distinguish between the strongly deformed, ca. 7.1–6.5 Ma redbeds of the Upper Vizcachera Formation below the Coranzulí Ignimbrite (6.6 Ma) and the overlying, largely undeformed, ca. 5.6–3.4 Ma deposits of the Pastos Chicos Formation.

Figure 3. Radial plots of single-grain apatite fission track age data and track length histograms (non-projected) for vertical profiles (a) COB—northern Sierra de Cobres; (b) SC—southern Sierra de Cobres; (c) SUS—Susques; (d) ST—Sierra de Tanque. For samples with $P(\chi^2) \geq 5\%$ the pooled age is reported, otherwise the central age (*) is used. $P(\chi^2)$—chi-square probability; n—number of individual crystals dated and individual confined tracks measured per sample; mean—mean track length; SD—standard deviation; Rel—relative. Note that estimates of mean track length may not be robust for samples with a small number of track length measurements.

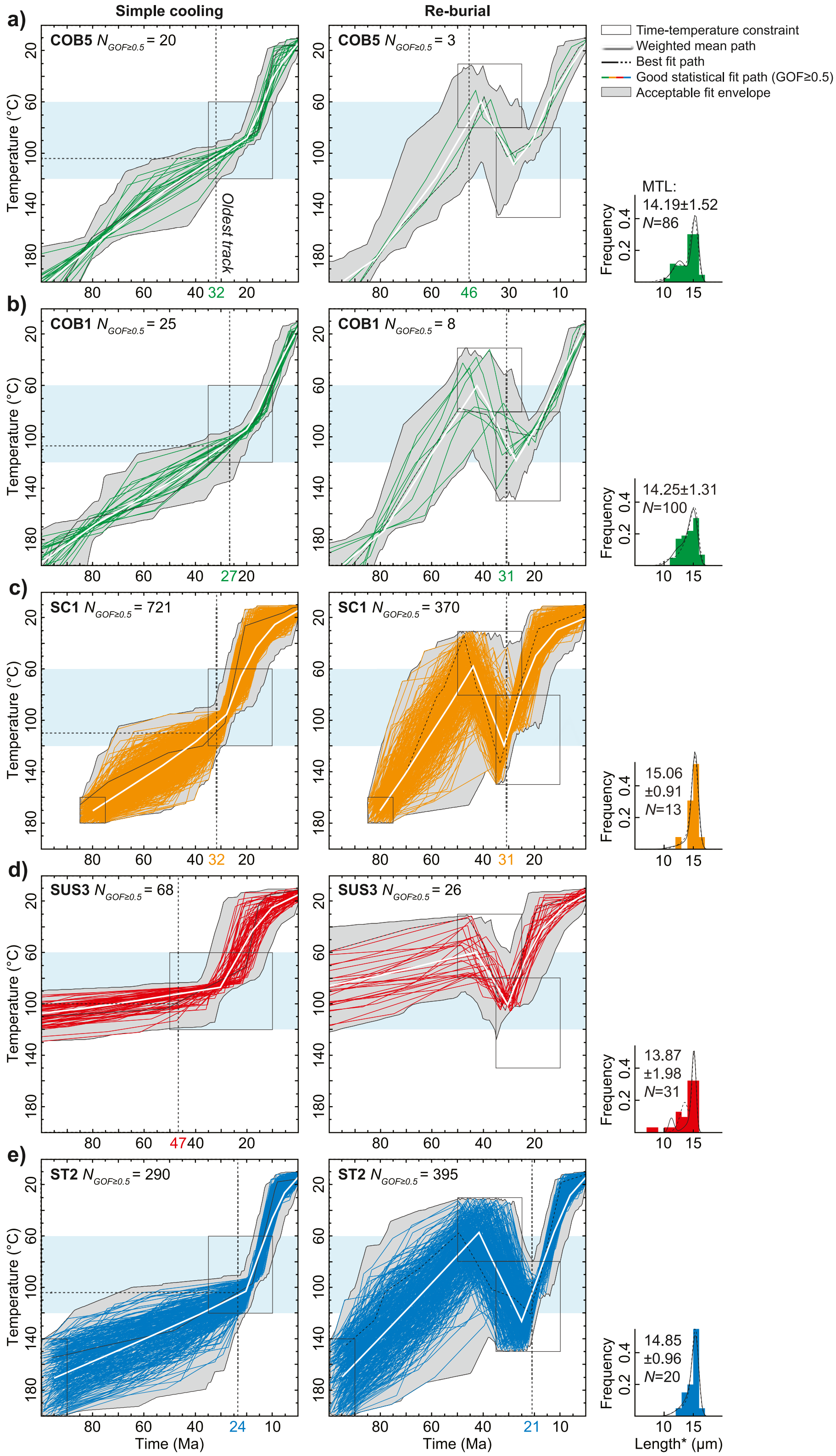

Figure 5. Representative thermal history models from simple-cooling (left side) and reheating inversions (right side) and measured and modeled AFT length distributions from: (a–b) southern Sierra de Cobres (COB); (c) northern Sierra de Cobres (SC); (d) northern Sierra de Cobres west of Cobres Fault (SUS); (e) Sierra de Tanque (ST). *N*—number of lengths measured; MTL and *—mean track length (c-axis projected); GOF—goodness of fit (GOF ≥ 0.5—good fit; GOF ≥ 0.05—acceptable fit).

Table 2
Summary of U–Pb Zircon Age Constraints

Sample ID	Latitude (°S)	Longitude (°W)	Elevation (m)	Lithology	Age (Ma)	2σ	MSWD	Grains
SUS-060319-5	23.42313	66.49001	4,004	Pastos Chicos Fm.	3.40	0.02	1.23	28/40
SUS-070319-4	23.57485	66.42392	3,730	Pastos Chicos Fm.	3.53	0.06	1.03	4/40
SUS-060319-4	23.42313	66.49001	4,004	Pastos Chicos Fm.	3.93	0.08	2.05	5/40
SUS-070319-2	23.51021	66.42768	3,710	Pastos Chicos Fm.	3.97	0.04	2.15	30/40
SUS-110313-2	23.42426	66.27299	3,800	Pastos Chicos Fm.	4.78	0.03	1.36	4/40
SUS-070319-3	23.51848	66.41652	3,711	Pastos Chicos Fm.	5.58	0.04	1.90	29/40
SUS-070319-1	23.42146	66.38375	3,596	Upper Vizcachera Fm.	6.51	0.07	2.22	14/40
SUS-110313-1	23.40151	66.35844	3,630	Upper Vizcachera Fm.	6.86	0.04	1.80	29/41
VA-1	23.40149	66.35861	3,600	Upper Vizcachera Fm.	7.03	0.06	2.23	11/48
SUS-060319-2	23.36659	66.36095	3,685	Upper Vizcachera Fm.	7.03	0.04	2.00	28/40
SUS-060319-1	23.37396	66.36880	3,633	Upper Vizcachera Fm.	7.06	0.11	–	2/40[a]

[a]U–Pb zircon maximum depositional age.

5. Discussion

5.1. Cooling History of the Pastos Chicos Basin

Most of our thermal inversion models do not allow an interpretation of the thermal history of the mountain ranges bordering the Pastos Chicos Basin in terms of an Eocene reheating scenario (except COB5, SUS3, and SUS4). This seems contradictory given the presence of the regionally widespread Eo-Oligocene Casa Grande Formation in the neighboring basins of the Puna (up to about 1 km thick, e.g., Gangui & Götze, 1996; Henríquez et al., 2020, 2022; López Steinmetz & Galli, 2015; Seggiaro et al., 2015) and the Eastern Cordillera (ca. 700 and 1,400 m thick in the Casa Grande and Cianzo basins, Montero-López et al., 2018; Siks & Horton, 2011). Yet, there are no documented outcrops of the Casa Grande Formation to suggest that the Pastos Chicos Basin was also buried beneath thick Eo-Oligocene strata (Figure 2). In this context, we refrain here from a detailed discussion of an Eocene reburial episode and instead focus on the results of our simple cooling inversions, whose thermal history largely overlaps with the final cooling history of the reheating inversions (Figure 5 and Figure S2–S5 in Supporting Information S1).

In the following, we estimate the onset of exhumation considering the range of good-fit model solutions of the highest and/or most reliable samples from each elevation transect, that is, COB5, SC1, SUS3, and ST2 (Figure 5).

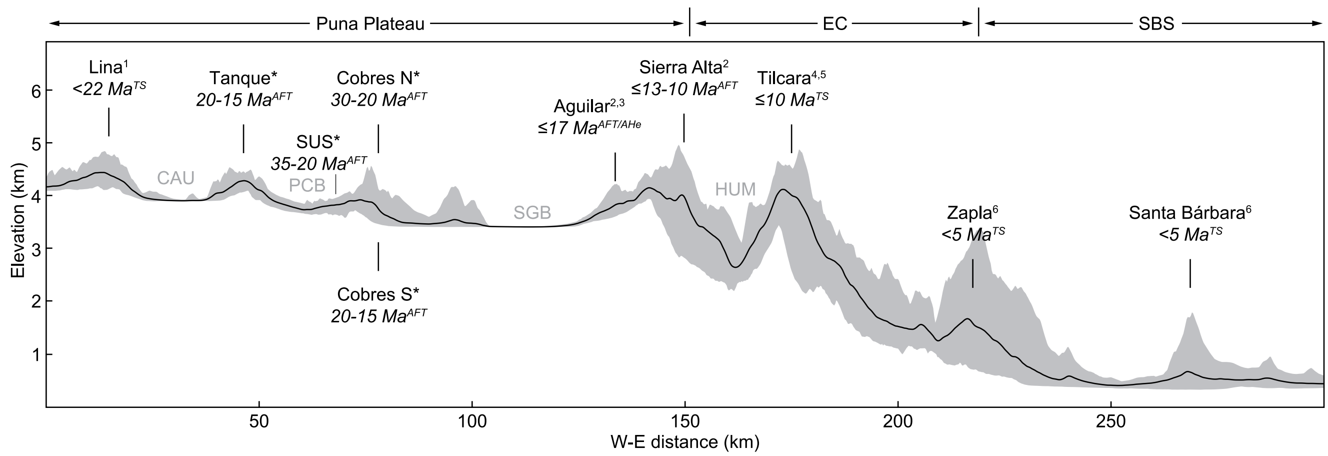

Figure 6. Topographic swath profile (ca. 40 km wide) showing average (black line) and max/min (gray envelope) elevation across the eastern Andean margin in North-western Argentina at ca. 23.5°S showing times of pronounced Cenozoic deformation: (*) this study; (1) Henríquez et al. (2020); (2) Deeken et al. (2005); (3) Lapiana (2021); (4) Siks and Horton (2011); (5) Pingel et al. (2013); (6) Kley and Monaldi (2002). Methods for each constraint: TS–tectonosedimentary; AFT–apatite fission track; AHe–apatite (U-Th)/He thermochronology. Location of the swath profile is shown in Figure 1.

Thermal solutions from the SUS3 sample, located west of the Cobres Fault, indicate that final exhumation of the associated block commenced at 35–20 Ma. Modeling results from the SC and SUS samples agree well and indicate rapid exhumation of the northern Sierra de Cobres around 30 Ma. The southern COB transect records slightly delayed cooling of the southern Sierra de Cobres (20–15 Ma), possibly resulting from southward-propagating faulting along the Cobres Fault. Final exhumation of the Sierra de Tanque began at 20–15 Ma.

Several of our thermal models suggest that rapid cooling was followed by early attainment of near-surface conditions around 20 Ma (SC1 and SUS3) and 10 Ma (COB5 and ST2) associated with much lower cooling rates. As previous studies have shown, this may be related to the removal of easily erodible sediments overlying resistant bedrock (e.g., Deeken et al., 2006; Sobel & Strecker, 2003). As rock uplift continues, more resistant bedrock is exposed, resulting in a decrease in exhumation while surface uplift increases. Attainment of near-surface temperatures at the northern Sierra de Cobres by 20 Ma approximately corresponds with the onset of deformation in the adjacent Sierra de Tanque and with uplift of the Sierra de Lina about 35 km to the west sometime after 22 Ma (Figures 1 and 6, Henríquez et al., 2020). Alternatively, reduced cooling rates may also indicate episodes of tectonic quiescence; however, the fact that we observe deformed basin strata up to 6.5 Ma suggests that shortening, and thus rock uplift, continued in the area of the Pastos Chicos Basin well into the late Miocene.

In summary, our thermochronology combined with published data suggest that final exhumation and deformation in the Pastos Chicos Basin began between ca. 30 and 20 Ma (late Oligocene) in the eastern Sierra de Cobres, propagated westward to the Sierra de Tanque and Sierra de Lina by ca. 20 Ma (early Miocene, Henríquez et al., 2020), and then shifted eastward (Figure 6). For example, (a) AFT thermal modeling suggests exhumation of the Sierra Aguilar to the east at about 20–16 Ma (Deeken et al., 2005; Henríquez et al., 2020; Lapiana, 2021); followed by (b) the exhumation of the Sierra Alta (15–10 Ma, Deeken et al., 2005; Henríquez et al., 2022); (c) deformation associated with uplift of the Aparzo and Tilcara ranges by ca. 10 Ma (Lapiana, 2021; Siks & Horton, 2011), and finally (d) the deformation of sectors of the Santa Bárbara System after 5 Ma (including the Zapla anticline, Kley & Monaldi, 2002). Thus, although deformation ultimately shifted eastward, its progression toward the foreland was diachronous. Note that this diachronous development is much more pronounced farther south, especially in the Eastern Cordillera south of 24°S (Mio-Pliocene) and during the Oligocene south of 26°S (e.g., Hain et al., 2011; Pearson et al., 2013; Zapata et al., 2020).

5.2. Mio-Pliocene Basin Evolution

So far, the chronostratigraphy of the Pastos Chicos Basin has been mainly tied to a limited set of K–Ar dates (and stratigraphic correlation) originating from the adjacent Olaroz/Cauchari Basin to the west and from the southernmost Pastos Chicos Basin (e.g., Schwab, 1973; Schwab & Lippolt, 1976). Using our results from thermal modeling and U–Pb zircon geochronology, we refine the stratigraphy of the Pastos Chicos Basin and reconstruct the tectonic-sedimentary evolution of this region on the Puna Plateau.

Considering the possible lag times between the thermochronologic signal and accelerated surface uplift (discussed in Section 5.1), topographic growth of ranges bounding the Pastos Chicos Basin, and thus development of significant sedimentary accommodation space, likely occurred sometime after the modeled onset of final exhumation (30 and 20 Ma). This may be indicated by the oldest Pastos Chicos Basin strata, the late Miocene redbeds of the Upper Vizcachera Formation that unconformably overlie deformed Ordovician basement rocks (e.g., Figure 7). As older sedimentary strata appear to be missing, these Miocene strata (Upper Vizcachera Formation) could represent an erosional response to surface uplift.

The Upper Vizcachera Formation in the Pastos Chicos Basin is mainly composed of fine-grained, continental, fluvial redbeds and intercalated volcanic ash layers. Most of the outcrops of this unit are strongly deformed and show a basal unconformable contact with the Ordovician basement. Our U–Pb zircon ages constrain deposition of this unit to >7–6.5 ± 0.1 Ma, consistent with the timing of the eruption of the Coranzulí volcanic complex and the regionally widespread emplacement of ignimbrites at about 6.6 ± 0.2 Ma (Seggiaro et al., 2019). Subsequently, the Pastos Chicos Formation was deposited. U–Pb zircon ages from ash deposits indicate that the Pastos Chicos Formation was deposited between at least 5.6 and 3.4 Ma. Field observations indicate that this unit consists primarily of coarse-grained sand and conglomerates deposited in alluvial fans sourced from the Sierra de Tanque to the west. At several locations corresponding to more distal sectors these alluvial fan deposits interfinger with well-stratified and undeformed layers of fine-grained, fluvio-lacustrine redbeds similar to the

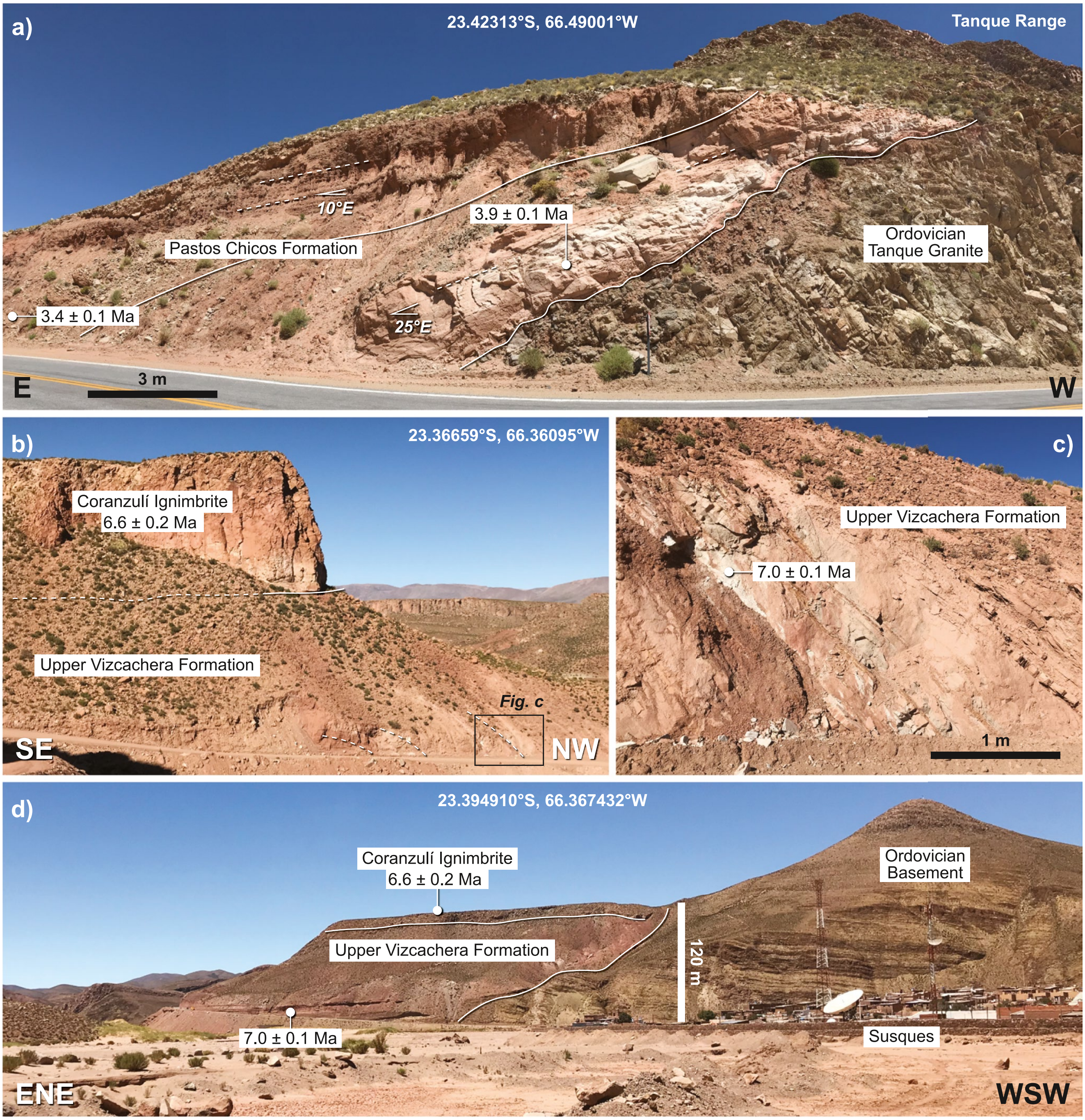

Figure 7. Field photos from the basin filling Upper Vizcachera and Pastos Chicos formations. (a) Unconformity between the Tanque granite and tilted sands and conglomerates of the Pliocene Pastos Chicos Formation on the western margin of the Pastos Chicos Basin. (b and c) Deformed late Miocene strata of the upper Vizcachera Formation unconformably overlain by the undeformed Coranzulí ignimbrite near the town of Susques. (d) Undeformed strata of the Upper Vizcachera Formation filling a paleotopography formed in the Ordovician basement, overlain by the Coranzulí ignimbrite.

Upper Vizcachera Formation. The ignimbrite and overlying Pastos Chicos Formation are mostly undeformed, suggesting that basin-internal deformation largely ceased around 6.6 Ma. Only along the western basin margin did deformation continue until at least 3.4 Ma, as indicated by tilted strata of the Pastos Chicos Formation that are part of a buttress unconformity (Figure 7).

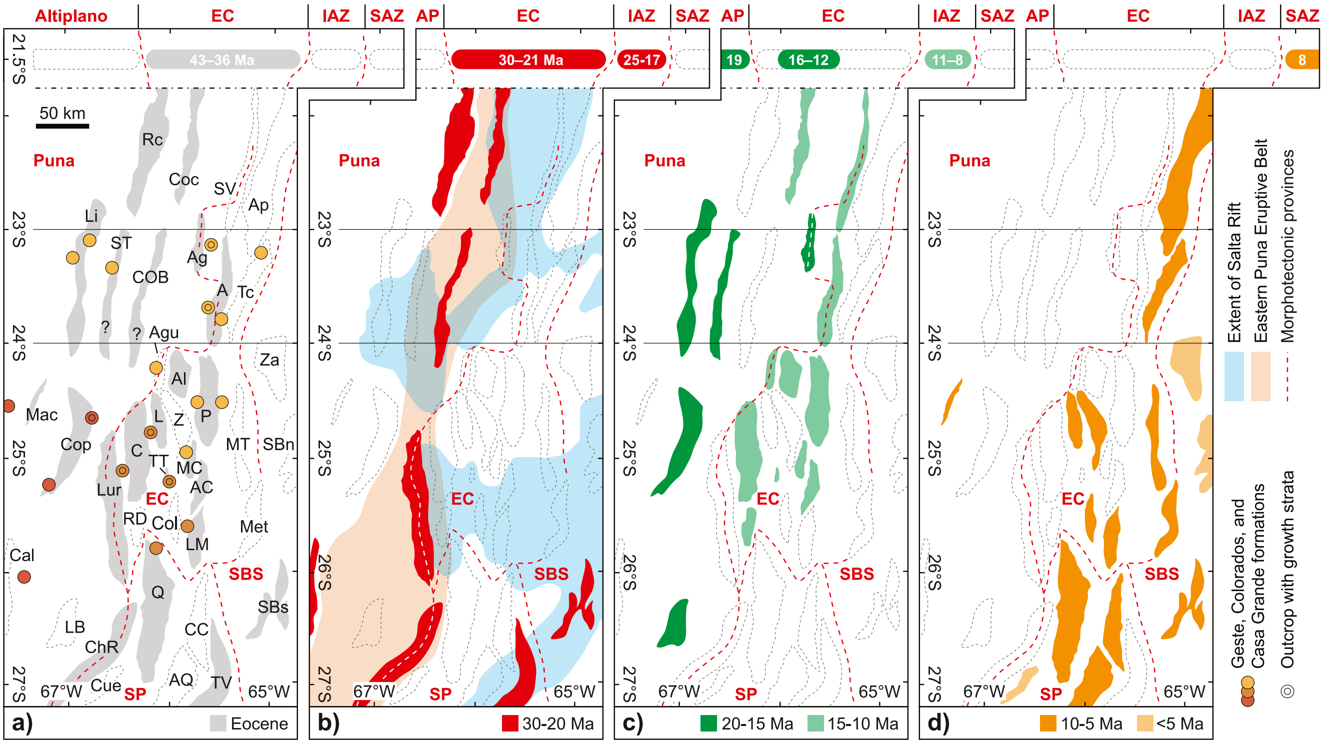

Figure 8. Schematic maps of north-western Argentina showing the spatio-temporal distribution of the deformation for four time periods based on our regional compilation of deformation onset in NW Argentina. For more information and references, see Table S6 in Supporting Information S2: (a) Eocene (gray); (b) Oligo-Miocene (red); (c) Miocene (green); (d) Mio-Pliocene (orange). Each map is provided with a spatio-temporal representation of the onset of deformation in southern Bolivia at 21.5°S (colored bars, numbers indicate time of deformation in Ma). Ranges: Rc—Rinconada; Coc—Cochinoca/Escaya; SV—Santa Victoria; Ap—Aparzo; Li—Lina; ST—Tanque; COB—Cobres; Ag—Aguilar; A—Alta/Mal Paso; Tc—Tilcara; Za—Zapla; Agu—Aguada; Al—Almagro; P—Pascha; MT—Mojotorro; SBSn—northern Santa Bárbara System (24°–25°S); Mac—Macón; Cop—Copalayo; C—Cachi-Palermo; L—Lampasillos; Z—Zamanca; MC—Malcante; Lur—Luracatao; RD—Runno-Durazno; TT—TinTin; Col—Colorados; LM—Leon Muerto; AC—Aguas de Castilla; Met—Metán; Cal—Calalaste; LB—Lagua Blanca; ChR—Chango Real; Cue—Cuevas; Q—Quilmes; AQ—Aconquija; CC—Calchaquí; TV—Tafi del Valle; SBSs—southern Santa Bárbara System (26°–27°S). Provinces: AP—Altiplano; EC—Eastern Cordillera; IAZ—Inter Andean Zone; SAZ—Subandean Zone; SBS—Santa Bárbara System; SP—Sierras Pampeanas.

5.3. Regional Implications

Although our data do not unequivocally demonstrate Eocene deformation at the location of the present-day Sierra de Cobres and Sierra de Tanque, we consider it highly unlikely that these areas were not deformed at that time, given the large spatial extent of contemporaneous deformation and the position of the two ranges within this extensive deformation zone (Figure 8). For example, during the middle Eocene, the present-day Sierra de Cobres was aligned along a deformation zone that extended 600 km from the Tupiza area in southern Bolivia at 21.5°S to the Sierra Chango Real at 27°S (Figure 8a, Coutand et al., 2001; Deeken et al., 2006; Ege et al., 2007; Payrola et al., 2009). Likewise, the neighboring Sierra de Tanque was aligned with the Sierra de Rinconada and Filo de Copalayo ranges, to the north and south, respectively, which also record Eocene deformation (Carrapa & DeCelles, 2008; López Steinmetz & Montero-López, 2019). Across-strike, Eocene deformation affected a region more than 300 km wide that presently comprises the northern Puna Plateau. From west to east, mountain ranges with documented Eocene deformation at the latitude of the Sierra de Tanque and Sierra de Cobres (ca. 23°–24°S) include the Cordillera de Domeyko in northern Chile at ca. 69°W (e.g., Arriagada et al., 2006; Maksaev, 1990; Maksaev & Zentilli, 1999; Mpodozis et al., 2005); the Sierra de Lina at 66.8°W (Henríquez et al., 2020); and the Sierra Aguilar and Sierra Alta as part of the present-day Eastern Cordillera (Montero-López et al., 2018, 2021). Including the studies listed above, many researchers have documented Eocene deformation throughout north-western Argentina and northern Chile with an area extending from approximately 22° to 27°S and from 69° to 65°W (Figure 8a, e.g., del Papa et al., 2013; Henríquez et al., 2020, 2022; Hongn et al., 2007; Montero-López et al., 2021; Payrola et al., 2020). A more comprehensive list of references used to determine the onset of deformation on a more regional scale (incl., Aramayo et al., 2017; del Papa et al., 2021; Hongn et al., 2011; Montero-López et al., 2017; Reiners et al., 2015; Reynolds et al., 2000; Vezzoli et al., 2012)

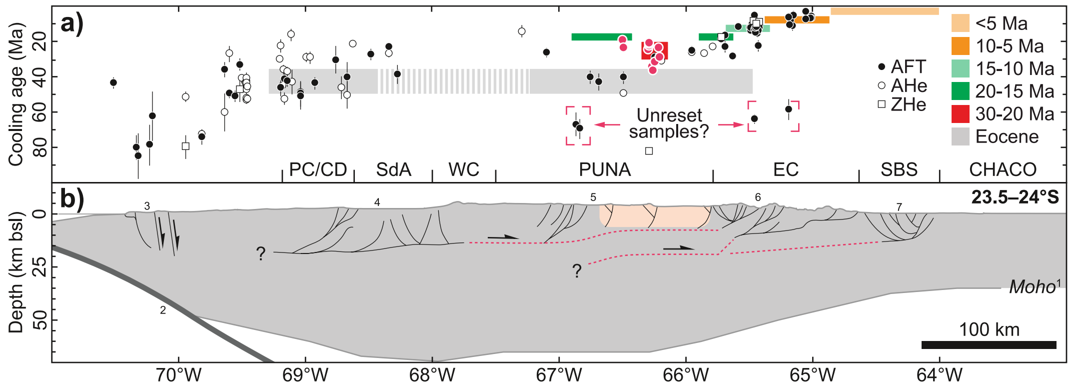

Figure 9. (a) Apatite fission track (AFT) (filled circles), apatite (U-Th)/He thermochronology (AHe) (open circles), and zircon (U–Th)/He thermochronology (ZHe) (open squares) cooling ages from 23° to 24°S plotted against longitude (Stalder et al., 2020; this study). Red circles represent the cooling ages from this study and colored bars show the extent of deformation onset in different time periods as discussed in the text. (b) Schematic regional cross sections through the Andes at 23°–24°S using data from: (1) Ibarra et al. (2019); (2) Hayes et al. (2018); (3) Allmendinger and González (2010); (4) Martínez et al. (2021); (5) Seggiaro et al. (2015); (6) González et al. (2003); (7) Kley and Monaldi (2002).

is provided in Table S6 in Supporting Information S2 and a graphical representation of the data is shown in Figures 8 and 9.

As noted above, deformation was virtually ubiquitous during the Eocene in an area that presently constitutes the north-western Argentine Andes (Figure 8a). After the widespread deposition of early foreland strata and the associated burial of formerly partially exhumed bedrock, deformation appears to have been renewed during the early Oligocene and early Miocene, between 30 and 20 Ma. For example, the Sierra de Rinconada (28 Ma, Ege et al., 2007), Sierra de Cobres (30 Ma, this study), Cumbres de Luracatao (23 Ma, Coutand et al., 2006), and Sierra Chango Real (30 Ma, Coutand et al., 2001) formed a narrow, 600-km-long, and approximately north-south trending belt of deformation. Hence, compared to the previously discussed extent of the Eocene broken foreland, deformation during the early Oligocene and early Miocene appears much more localized (Figure 8b). Importantly, the long sub-meridional belt of localized deformation largely coincides with at least two well-known zones of crustal weakness that partially overlap (Figure 8b). First, the Ordovician Eastern Puna Eruptive Belt (Coira et al., 1999; Méndez et al., 1973), a magmatic arc system related to the Famatinian orogeny, which runs from the Sierra de Cochinoca/Escaya Range in the northern Puna southward through the Sierra de Cobres and Sierra de Tanque to the Cumbres de Luracatao and Sierra Chango Real. The second zone corresponds to the western and northern branches of the Salta Rift (e.g., Marquillas et al., 2005; Marquillas & Salfity, 1988). Many Cenozoic structures located within these two zones have been associated with the reactivation of Paleozoic shear zones and planar metamorphic fabrics and inversion of Cretaceous normal faults (e.g., Grier et al., 1991; Hongn et al., 2010; Hongn & Riller, 2007; Kley et al., 2005). Exceptions from the narrow deformation pattern are the Sierra de Calalaste within the present-day Puna Plateau (Carrapa et al., 2005; Kraemer et al., 1999; Zhou et al., 2017), the Tafi del Valle Range in the northern Sierras Pampeanas (Zapata et al., 2020), and the Sierra de Candelaria in the southern Santa Bárbara System (Zapata et al., 2020). However, all these ranges are located south of 26°S, at the latitude of the northern Sierras Pampeanas and are either associated with regions directly bordering the Eastern Puna Eruptive Belt or located within the southern branch of the Salta Rift (Figure 8b).

Between 20 and 15 Ma renewed deformation and exhumation are documented largely west of the aforementioned early Oligo-Miocene deformation belt and affected the Sierra de Tanque (this study) and Sierra de Lina (Henríquez et al., 2020), as well as the Sierra Laguna Blanca of the southern Puna Plateau (Zhou et al., 2017). Onset of deformation of the intervening Filo de Copalayo Range (≥15 Ma) is inferred from the results of Carrapa et al. (2009), who determined the exhumation of the former sedimentary cover of the range (Geste Formation) using detrital apatite (U-Th)/He (AHe) dating. To the east, thermal modeling suggests rapid exhumation of the Sierra Aguilar between 20 and 16 Ma (Lapiana, 2021). Onset of deformation between 15 and 10 Ma was concentrated in the southern part of the Eastern Cordillera (Andriessen & Reutter, 1994; Carrapa et al., 2011; Deeken et al., 2006; Payrola et al., 2021; Pearson et al., 2012, 2013; Pingel et al., 2019) and has affected the borders of all major intermontane basins in north-western Argentina until the present day, including the Humahuaca and

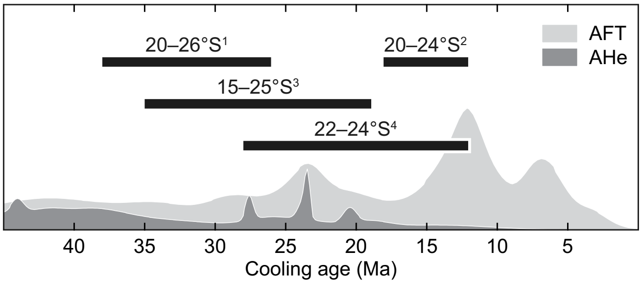

Figure 10. Probability density plot of apatite fission track (AFT) and apatite (U-Th)/He thermochronology (AHe) cooling ages from 23° to 24°S (Stalder et al., 2020; this study, data shown in Figure 9) illustrating the mismatch between deformation and proposed flat-slab subduction periods: (1) Haschke et al. (2002); (2) Ramos and Folguera (2009); (3) Horton (2018); (4) Kay et al. (1999).

Toro basins, as well as the basins of the greater Calchaquí region. Between 10 and 5 Ma, renewed deformation in the Puna Plateau appears to be absent and tectonic activity shifted eastward to the present-day Eastern Cordillera (Carrapa et al., 2011; DeCelles et al., 2011; Lapiana, 2021; Pearson et al., 2013; Pingel et al., 2013, 2020; Rahl et al., 2018; Siks & Horton, 2011) and the Sierras Pampeanas (Löbens et al., 2013; Mortimer et al., 2007; Sobel & Strecker, 2003; Strecker et al., 1989) and, to some extent, the southern Santa Bárbara System (Arnous et al., 2020; Zapata et al., 2020). Interestingly, the eastern boundary of the Eastern Cordillera deformed synchronously at ca. 10 Ma along its entire length from the Tilcara Ranges (23.5°S, Siks & Horton, 2011; Lapiana, 2021) in the north to the Sierra Mojotorro (25°S, Pearson et al., 2013) and Sierra Metán in the south (25.5°S, Hain et al., 2011). An exception to this pattern appears to be the Sierra Macón in the central Puna, whose final exhumation began around 10 Ma (Carrapa et al., 2009), possibly in response to partial removal of the underlying lithosphere (DeCelles et al., 2015). Finally, the latest initiation of deformation since 5 Ma is mainly observed in the Santa Bárbara System. This is exemplified by the post-5 Ma growth of the Zapla anticline and uplift in the northern Santa Bárbara System at ca. 24°S (Kley & Monaldi, 2002).

Overall, the spatio-temporal pattern of basement deformation in the Pastos Chicos Basin and adjacent regions at 23°–24°S seems incompatible with the notion of a steadily eastward-propagating deformation front as would be expected in a classical orogenic-wedge system (e.g., Dahlen, 1990). Although deformation ultimately migrated eastward during the evolution of this sector of the Andes, propagation of deformation toward the foreland was diachronous (Figures 8 and 9). Importantly, the style of deformation described here records spatially disparate uplifts in a formerly contiguous foreland basin, where maximum horizontal compressive stresses were localized at inherited crustal fault zones and drove them toward failure, resulting in deformation distributed over a broad area extending far into the back-arc of the orogen. This spatio-temporal pattern of range formation and basin fragmentation is akin to the pattern of deformation observed in a broken foreland, analogous to parts of the Colombian and Peruvian Andes (e.g., Mora et al., 2006; Parra et al., 2009; Ramos & Folguera, 2009), the Miocene to Recent basement uplifts in the Sierras Pampeanas and Santa Bárbara System broken-foreland provinces of the Andes (e.g., Allmendinger et al., 1983; Hain et al., 2011; Hongn et al., 2007; Mortimer et al., 2007), the Cretaceous to Eocene Laramide province of North America (e.g., Jordan & Allmendinger, 1986), the Tian Shan (e.g., Sobel & Dumitru, 1997; Sobel et al., 2003), and the Qilian Shan of China (e.g., Tapponnier et al., 1990).

The development of a broken foreland is often related to shallow subduction (e.g., Jordan et al., 1983). For example, in the southern Bolivian Andes at 21°S, middle Eocene to early Oligocene initiation of horizontal crustal shortening and rock uplift in the Bolivian Eastern Cordillera, co-occurred with proposed episodes of shallow subduction (e.g., Anderson et al., 2018). Based on the Eocene deformation pattern observed in the Argentine Andes (Figure 8a), one might be tempted to project the flat slab further south. However, the presence of an Eocene magmatic arc in the Cordillera de Domeyko (e.g., Haschke et al., 2002) precludes flat subduction at that time. Several authors have suggested post-Eocene shallow subduction at different times in the Andean section between 23° and 24°S (Figure 10). For example, Haschke et al. (2002) observe a magmatic gap between 38 and 26 Ma associated with flat-slab subduction at 20°–26°S. Similarly, Kay et al. (1999) proposed a magmatic gap between 28 and 12 Ma at 22°–24°S. Based on deformation patterns, Horton (2018) proposed flat-slab subduction between 35 and 20 Ma at 15°–25°S. Finally, Ramos and Folguera (2009) proposed a period of flat-slab subduction between 18 and 12 Ma at ca. 20°–24°S. Yet, none of these proposed time periods seem to fit with the observed crustal deformation patterns (Figure 10). Thus, instead of being attributed to enhanced plate coupling during flat-slab subduction, the observed non-systematic (spatially disparate and diachronous), thick-skinned thrusting may be rather due to heterogeneous deformation of a large orogenic wedge (Armijo et al., 2010) intermittently aided by slip on pre-existing crustal structural discontinuities such as the Paleozoic shear zones and Cretaceous normal faults of the north-west Argentine basement.

6. Conclusions

The spatio-temporal information on deformation in the northern Puna and adjacent provinces to the east (Eastern Cordillera and Santa Bárbara System), drawn from new AFT and ZHe thermochronology and inverse modeling combined with published data, allows us to assess the tectonic evolution across the eastern Andean margin since the Eocene. After widespread deformation across almost the entire Puna Plateau during the Eocene, deformation in north-western Argentina was concentrated in a narrow belt of weakened basement (at the position of the Eastern Puna Eruptive Belt) during the Oligocene to early Miocene that more or less follows the present-day eastern margin of the Puna Plateau. Following initial westward migration of tectonism in the early Miocene, deformation shifted more systematically eastward into the present-day Santa Bárbara System, whereas south of 24°S spatio-temporal patterns in deformation show a rather diachronous orogenic development, likely associated with pre-existing crustal heterogeneities.

Zircon U-Pb geochronology of deformed and undeformed ash-bearing strata and field observations are used to specify the tectonic-sedimentary evolution of the Pastos Chicos Basin. Consistent with thermal models, deposition began with the Upper Vizcachera Formation prior to 7 Ma. These units were deformed until about 6.5 Ma, when the regionally extensive Coranzulí Ignimbrite was emplaced (6.6 ± 0.2 Ma). This ignimbrite and subsequent basin fills of the Pastos Chicos Formation (5.6–3.4 Ma) have remained largely undeformed, suggesting that tectonic shortening ceased in this sector of the Andes, consistent with increased deformation in the Eastern Cordillera and Santa Bárbara System.

Data Availability Statement

Data from this study can be found in Supporting Information and on figshare at https://doi.org/10.6084/m9.figshare.20209865.v1.

Acknowledgments

This research was funded by the Deutsche Forschungsgemeinschaft (DFG) Grant STR373/21-1 and STR373/16-1 to M. Strecker. Additional support came from the DFG Grant STR373/34-1 and the Brandenburg Ministry of Sciences, Research and Cultural Affairs, Germany, within the framework of the international research training group IGK2018 SuRfAce processes, TEctonics and Georesources: The Andean foreland basin of Argentina (StRATEGy). Additional support came from the Blaustein Fund, the Fulbright Foundation, and the France-Stanford Center for Interdisciplinary Studies to I. Coutand. The authors are grateful to T. Dumitru for supporting the AFT work at the Stanford University. Originally prepared as part of A. Deeken's dissertation, this work is dedicated to her. Finally, the authors thank Sarah W. M. George and an anonymous reviewer for their constructive comments on this study. Open Access funding enabled and organized by Projekt DEAL.

References

Adelmann, D. (2001). *Känozoische Beckenentwicklung in der südlichen Puna am Beispiel des Salar de Antofolla (NW-Argentinien)* (PhD thesis). Freie Universität Berlin.

Allmendinger, R. W., & González, G. (2010). Invited review paper: Neogene to Quaternary tectonics of the coastal Cordillera, northern Chile. *Tectonophysics*, *495*, 93–110. https://doi.org/10.1016/j.tecto.2009.04.019

Allmendinger, R. W., & Gubbels, T. (1996). Pure and simple shear plateau uplift, Altiplano-Puna, Argentina and Bolivia. *Tectonophysics*, *259*(1–3), 1–13. https://doi.org/10.1016/0040-1951(96)00024-8

Allmendinger, R. W., Ramos, V. A., Jordan, T. E., Palma, M., & Isacks, B. L. (1983). Paleogeography and Andean structural geometry, northwest Argentina. *Tectonics*, *2*, 1–16. https://doi.org/10.1029/tc002i001p00001

Andersen, T. (2002). Correction of common lead in U–Pb analyses that do not report ^{204}Pb. *Chemical Geology*, *192*(1–2), 59–79. https://doi.org/10.1016/s0009-2541(02)00195-x

Anderson, R. B., Long, S. P., Horton, B. K., Thomson, S. N., Calle, A. Z., & Stockli, D. F. (2018). Orogenic wedge evolution of the Central Andes, Bolivia (21°S): Implications for Cordilleran cyclicity. *Tectonics*, *37*(10), 3577–3609. https://doi.org/10.1029/2018tc005132

Andriessen, P. A. M., & Reutter, K.-J. (1994). K-Ar and fission track mineral age determination of igneous rocks related to multiple magmatic arc systems along the 23°S latitude of Chile and NW Argentina. In K.-J. Reutter, E. Scheuber, & P. J. Wigger (Eds.), *Tectonics of the Southern Central Andes: Structure and evolution of an active continental margin* (pp. 141–153). Springer. https://doi.org/10.1007/978-3-642-77353-2_10

Aramayo, A. J., Hongn, F. D., & del-Papa, C. E. (2017). Acortamiento Paleógeno en el tramo medio de los Valles Calchaquíes: Depositación sintectónica de la Formación Quebrada de los Colorados. *Revista de la Asociación Geológica Argentina*, *74*, 524–536.

Armijo, R., Rauld, R., Thiele, R., Vargas, G., Campos, J., Lacassin, R., & Kausel, E. (2010). The West Andean thrust, the San Ramón fault, and the seismic hazard for Santiago, Chile. *Tectonics*, *29*(2), TC2007. https://doi.org/10.1029/2008tc002427

Arnous, A., Zeckra, M., Venerdini, A., Alvarado, P., Arrowsmith, R., Guillemoteau, J., et al. (2020). Neotectonic activity in the low-strain broken foreland (Santa Bárbara System) of the North-Western Argentinean Andes (26°S). *Lithosphere*, *2020*(1), 8888588. https://doi.org/10.2113/2020/8888588

Arriagada, C., Cobbold, P. R., & Roperch, P. (2006). Salar de Atacama basin: A record of compressional tectonics in the Central Andes since the mid-Cretaceous. *Tectonics*, *25*(1), TC1008. https://doi.org/10.1029/2004tc001770

Bahlburg, H. (1990). *The Ordovician basin in the Puna of NW Argentina and N Chile: Geodynamic evolution from back-arc to foreland basin*. Schweizerbart Science Publishers.

Bahlburg, H., Berndt, J., & Gerdes, A. (2016). The ages and tectonic setting of the Faja Eruptiva de la Puna Oriental, Ordovician, NW Argentina. *Lithos*, *256*, 41–54. https://doi.org/10.1016/j.lithos.2016.03.018

Benjamin, M. T., Johnson, N. M., & Naeser, C. W. (1987). Recent rapid uplift in the Bolivian Andes: Evidence from fission-track dating. *Geology*, *15*(7), 680–683. https://doi.org/10.1130/0091-7613(1987)15<680:rruitb>2.0.co;2

Browaeys, J. (2022). Linear fit with both uncertainties in x and in y (MATLAB Central File Exchange). Retrieved from https://www.mathworks.com/matlabcentral/fileexchange/45711-linear-fit-with-both-uncertainties-in-x-and-in-y

Caffe, P. J., & Coira, B. L. (2002). Chronostratigraphy of the San Juan de Oro Basin and its tectonic implications for the northern Puna during the Miocene. *Proceedings 5th International Symposium of Andean Geodynamics (ISAG 2002, Toulouse, France, 2002)*.

Carrapa, B., Adelmann, D., Hilley, G. E., Mortimer, E., Sobel, E. R., & Strecker, M. R. (2005). Oligocene range uplift and development of plateau morphology in the southern Central Andes. *Tectonics*, *24*(4), TC4011. https://doi.org/10.1029/2004tc001762

Carrapa, B., & DeCelles, P. G. (2008). Eocene exhumation and basin development in the Puna of northwestern Argentina. *Tectonics*, *27*(1), TC1015. https://doi.org/10.1029/2007tc002127

Carrapa, B., DeCelles, P. G., Reiners, P. W., Gehrels, G. E., & Sudo, M. (2009). Apatite triple dating and white mica ^{40}Ar/^{39}Ar thermochronology of syntectonic detritus in the Central Andes: A multiphase tectonothermal history. *Geology*, *37*(5), 407–410. https://doi.org/10.1130/g25698a.1

Carrapa, B., Strecker, M. R., & Sobel, E. R. (2006). Cenozoic orogenic growth in the Central Andes: Evidence from sedimentary rock provenance and apatite fission track thermochronology in the Fiambalá Basin, southernmost Puna Plateau margin (NW Argentina). *Earth and Planetary Science Letters*, *247*(1–2), 82–100. https://doi.org/10.1016/j.epsl.2006.04.010

Carrapa, B., Trimble, J. D., & Stockli, D. F. (2011). Patterns and timing of exhumation and deformation in the Eastern Cordillera of NW Argentina revealed by (U-Th)/He thermochronology. *Tectonics*, *30*(3), TC3003. https://doi.org/10.1029/2010tc002707

Coira, B., Kay, S. M., Pérez, B., Woll, B., Hanning, M., & Flores, P. (1999). Magmatic sources and tectonic setting of Gondwana margin Ordovician magmas, northern Puna of Argentina and Chile. *Special Papers – Geological Society of America*, *336*, 145–170. https://doi.org/10.1130/0-8137-2336-1.145

Coira, B., Kay, S. M., & Viramonte, J. (1993). Upper Cenozoic magmatic evolution of the Argentine Puna—A model for changing subduction geometry. *International Geology Review*, *35*(8), 677–720. https://doi.org/10.1080/00206819309465552

Cottle, J. M. (2014). In-situ U–Th/Pb geochronology of (urano)thorite. *American Mineralogist*, *99*(10), 1985–1995. https://doi.org/10.2138/am-2014-4920

Cottle, J. M., Burrows, A. J., Kylander-Clark, A., Freedman, P. A., & Cohen, R. S. (2013). Enhanced sensitivity in laser ablation multi-collector inductively coupled plasma mass spectrometry. *Journal of Analytical Atomic Spectrometry*, *28*(11), 1700–1706. https://doi.org/10.1039/c3ja50216c

Coutand, I., Carrapa, B., Deeken, A., Schmitt, A. K., Sobel, E. R., & Strecker, M. R. (2006). Propagation of orographic barriers along an active range front: Insights from sandstone petrography and detrital apatite fission-track thermochronology in the intramontane Angastaco basin, NW Argentina. *Basin Research*, *18*, 1–26. https://doi.org/10.1111/j.1365-2117.2006.00283.x

Coutand, I., Cobbold, P. R., Urreiztieta, M., Gautier, P., Chauvin, A., Gapais, D., et al. (2001). Style and history of Andean deformation, Puna Plateau, northwestern Argentina. *Tectonics*, *20*(2), 210–234. https://doi.org/10.1029/2000tc900031

Crowley, J. L., Schoene, B., & Bowring, S. A. (2007). U-Pb dating of zircon in the Bishop Tuff at the millennial scale. *Geology*, *35*(12), 1123–1126. https://doi.org/10.1130/g24017a.1

Dahlen, F. A. (1990). Critical Taper model of fold-and-thrust belts and Accretionary wedges. *Annual Review of Earth and Planetary Sciences*, *18*(1), 55–99. https://doi.org/10.1146/annurev.ea.18.050190.000415

Davis, S. J., Mulch, A., Carroll, A. R., Horton, T. W., & Chamberlain, C. P. (2009). Paleogene landscape evolution of the central North American Cordillera: Developing topography and hydrology in the Laramide forelandPaleogene landscape evolution of the central North American Cordillera. *GSA Bulletin*, *121*, 100–116. https://doi.org/10.1130/b26308.1

DeCelles, P. G., Carrapa, B., Horton, B. K., & Gehrels, G. E. (2011). Cenozoic foreland basin system in the Central Andes of northwestern Argentina: Implications for Andean geodynamics and modes of deformation. *Tectonics*, *30*(6), TC6013. https://doi.org/10.1029/2011tc002948

DeCelles, P. G., Carrapa, B., Horton, B. K., McNabb, J., Gehrels, G. E., & Boyd, J. (2015). The Miocene Arizaro Basin, Central Andean hinterland: Response to partial lithosphere removal? In P. G. DeCelles, M. N. Ducea, B. Carrapa, & P. A. Kapp (Eds.), *Geodynamics of a Cordilleran orogenic system: The Central Andes of Argentina and Northern Chile*. Geological Society of America. https://doi.org/10.1130/2015.1212(18)

DeCelles, P. G., & Horton, B. K. (2003). Early to middle Tertiary foreland basin development and the history of Andean crustal shortening in Bolivia. *GSA Bulletin*, *115*(1), 58–77. https://doi.org/10.1130/0016-7606(2003)115<0058:etmtfb>2.0.co;2

Deeken, A., Sobel, E. R., Haschke, M., & Riller, U. (2005). Age of initiation and growth pattern of the Puna Plateau, NW-Argentina, constrained by AFT thermochronology. *19th Colloquium on Latin American Geosciences, Abstract Volume Terra Nostra*, *5*(1), 39.

Deeken, A., Sobel, E. R., Haschke, M., Riller, U., & Strecker, M. R. (2006). Development of the southern Eastern Cordillera, NW Argentina, constrained by apatite fission track thermochronology: From early Cretaceous extension to middle Miocene shortening. *Tectonics*, *25*, TC6003. https://doi.org/10.1029/2005tc001894

del Papa, C., Hongn, F., Powell, J., Payrola, P., Do Campo, M., Strecker, M. R., et al. (2013). Middle Eocene-Oligocene broken-foreland evolution in the Andean Calchaqui Valley, NW Argentina: Insights from stratigraphic, structural and provenance studies. *Basin Research*, *25*(5), 574–593. https://doi.org/10.1111/bre.12018

del Papa, C., Payrola, P., Pingel, H., Hongn, F., Do Campo, M., Sobel, E. R., et al. (2021). Stratigraphic response to fragmentation of the Miocene Andean foreland basin, NW Argentina. *Basin Research*, *33*(6), 2914–2937. https://doi.org/10.1111/bre.12589

Dickinson, W. R., & Snyder, W. S. (1978). Laramide folding associated with basement block faulting in the Western United States. *Geological Society of America Memoir*, 355–366. https://doi.org/10.1130/mem151-p355

Donelick, R. A., Ketcham, R. A., & Carlson, W. D. (1999). Variability of apatite fission-track annealing kinetics: II. Crystallographic orientation effects. *American Mineralogist*, *84*(9), 1224–1234. https://doi.org/10.2138/am-1999-0902

Dumitru, T. A. (1993). A new computer-automated microscope stage system for fission-track analysis. *Nuclear Tracks and Radiation Measurements*, *21*(4), 575–580. https://doi.org/10.1016/1359-0189(93)90198-i

Echavarria, L., Hernández, R., Allmendinger, R., & Reynolds, J. (2003). Subandean thrust and fold belt of northwestern Argentina: Geometry and timing of the Andean evolution. *AAPG Bulletin*, *87*(6), 965–985. https://doi.org/10.1306/01200300196

Ege, H., Sobel, E. R., Scheuber, E., & Jacobshagen, V. (2007). Exhumation history of the southern Altiplano Plateau (southern Bolivia) constrained by apatite fission track thermochronology. *Tectonics*, *26*(1), TC1004. https://doi.org/10.1029/2005tc001869

Elger, K., Oncken, O., & Glodny, J. (2005). Plateau-style accumulation of deformation: Southern Altiplano. *Tectonics*, *24*(4), TC4020. https://doi.org/10.1029/2004tc001675

Ernst, W. G. (2010). Young convergent-margin orogens, climate, and crustal thickness—A Late Cretaceous–Paleogene Nevadaplano in the American Southwest? *Lithosphere-us*, *2*, 67–75. https://doi.org/10.1130/l84.1

Farley, K. A., Wolf, R. A., & Silver, L. T. (1996). The effects of long alpha-stopping distances on (U–Th)/He ages. *Geochimica et Cosmochimica Acta*, *60*(21), 4223–4229. https://doi.org/10.1016/s0016-7037(96)00193-7

Fernández, J., Bondesio, P., & Pascual, R. (1973). Restos de lepidosiren paradoxa (osteichthyes, dipnoi) de la Formacion Lumbrera (Eogeno, ¿Eoceno?) de Jujuy. *Ameghiniana*, *10*, 152–172.

Galbraith, R. F., & Laslett, G. M. (1993). Statistical models for mixed fission track ages. *Nuclear Tracks and Radiation Measurements*, *21*(4), 459–470. https://doi.org/10.1016/1359-0189(93)90185-c

Galetto, A., Georgieva, V., García, V. H., Zattin, M., Sobel, E. R., Glodny, J., et al. (2021). Cretaceous and Eocene rapid cooling phases in the Southern Andes (36°–37°S): Insights from low-temperature thermochronology, U-Pb geochronology, and inverse thermal modeling from Domuyo area, Argentina. *Tectonics*, *40*(6), e2020TC006415. https://doi.org/10.1029/2020tc006415

Galliski, M. A., & Viramonte, J. G. (1988). The Cretaceous paleorift in northwestern Argentina: A petrologic approach. *Journal of South American Earth Sciences*, *1*(4), 329–342. https://doi.org/10.1016/0895-9811(88)90021-1

Gangui, A. H., & Götze, H.-J. (1996). The deep structure of the Northern Puna (Argentina) – Constraints from 2D Seismik data and 3D Gravity modelling. *Actas XIII Congreso Geológico Argentino*, *2*, 545–565.

Gleadow, A. J. W., & Duddy, I. R. (1981). A natural long-term track annealing experiment for apatite. *Nuclear Tracks*, 5(1–2), 169–174. https://doi.org/10.1016/0191-278x(81)90039-1

González, M. A., Tchilinguirian, P., Pereyra, F. X., Ramallo, E. E., & Gonźalez, O. E. (2003). *Hoja Geológica 2366-IV, Ciudad de Libertador General San Martín, Provincias de Jujuy y Salta* (Boletín 274, p. 109). Instituto de Geología y Recursos Minerales, Servicio Geológico Minero Argentino.

Green, P. F. (1981). A new look at statistics in fission-track dating. *Nuclear Tracks*, 5(1–2), 77–86. https://doi.org/10.1016/0191-278x(81)90029-9

Grier, M. E., Salfity, J. A., & Allmendinger, R. W. (1991). Andean reactivation of the Cretaceous Salta rift, northwestern Argentina. *Journal of South American Earth Sciences*, *4*, 351–372. https://doi.org/10.1016/0895-9811(91)90007-8

Hain, M. P., Strecker, M. R., Bookhagen, B., Alonso, R. N., Pingel, H., & Schmitt, A. K. (2011). Neogene to Quaternary broken foreland formation and sedimentation dynamics in the Andes of NW Argentina (25°S). *Tectonics*, *30*(2), TC2006. https://doi.org/10.1029/2010tc002703

Haschke, M. R., Scheuber, E., Günther, A., & Reutter, K.-J. (2002). Evolutionary cycles during the Andean orogeny: Repeated slab breakoff and flat subduction? *Terra Nova*, *14*(1), 49–55. https://doi.org/10.1046/j.1365-3121.2002.00387.x

Hayes, G. P., Moore, G. L., Portner, D. E., Hearne, M., Flamme, H., Furtney, M., & Smoczyk, G. M. (2018). Slab2, a comprehensive subduction zone geometry model. *Science*, *362*(6410), 58–61. https://doi.org/10.1126/science.aat4723

Henríquez, S., DeCelles, P. G., Carrapa, B., & Hughes, A. N. (2022). Kinematic evolution of the central Andean retroarc thrust belt in northwestern Argentina and implications for coupling between shortening and crustal thickening. *GSA Bulletin*, *135*(1–2), 81–103. https://doi.org/10.1130/b36231.1

Henríquez, S., DeCelles, P. G., Carrapa, B., Hughes, A. N., Davis, G. H., & Alvarado, P. (2020). Deformation history of the Puna Plateau, Central Andes of northwestern Argentina. *Journal of Structural Geology*, *140*, 104133. https://doi.org/10.1016/j.jsg.2020.104133

Hongn, F., del Papa, C., Powell, J., Payrola, P., Petrinovic, I., & Mon, R. (2011). Fragmented Paleogene foreland basin in the Valles Calchaquíes, NW of Argentina. In J. A. Salfity & R. Marquillas (Eds.), *Cenozoic geology of the Central Andes of Argentina* (pp. 189–209). SCS Publisher.

Hongn, F., del Papa, C., Powell, J., Petrinovic, I., Mon, R., & Deraco, V. (2007). Middle Eocene deformation and sedimentation in the Puna-Eastern Cordillera transition (23°–26°S): Control by preexisting heterogeneities on the pattern of initial Andean shortening. *Geology*, *35*(3), 271–274. https://doi.org/10.1130/g23189a.1

Hongn, F., Mon, R., Petrinovic, I., del Papa, C., & Powel, J. (2010). Inversión y reactivación tectónicas Cretácico-Cenozoicas en el noroeste Argentino: Influenciade las heterogeneidades del basamento Neoproterozoico-Paleozoico inferior. *Revista de la Asociación Geológica Argentina*, *66*(1), 33–53. Retrieved from https://revista.geologica.org.ar/raga/article/view/841

Hongn, F. D., & Riller, U. (2007). Tectonic evolution of the western margin of Gondwana inferred from syntectonic emplacement of Paleozoic granitoid plutons in northwest Argentina. *The Journal of Geology*, *115*(2), 163–180. https://doi.org/10.1086/510644

Horton, B. K. (2018). Tectonic regimes of the central and southern Andes: Responses to variations in plate coupling during subduction. *Tectonics*, *37*(2), 402–429. https://doi.org/10.1002/2017tc004624

Horton, B. K., Hampton, B. A., Lareau, B. N., & Baldellón, E. (2002). Tertiary provenance history of the northern and central Altiplano (Central Andes, Bolivia): A detrital record of plateau-margin tectonics. *Journal of Sedimentary Research*, *72*(5), 711–726. https://doi.org/10.1306/020702720711

Hourigan, J. K., Reiners, P. W., & Brandon, M. T. (2005). U-Th zonation-dependent alpha-ejection in (U-Th)/He chronometry. *Geochimica et Cosmochimica Acta*, *69*(13), 3349–3365. https://doi.org/10.1016/j.gca.2005.01.024

Hurford, A. J., & Green, P. F. (1983). The zeta age calibration of fission-track dating. *Chemical Geology*, *41*, 285–317. https://doi.org/10.1016/s0009-2541(83)80026-6

Ibarra, F., Liu, S., Meeßen, C., Prezzi, C. B., Bott, J., Scheck-Wenderoth, M., et al. (2019). 3D data-derived lithospheric structure of the Central Andes and its implications for deformation: Insights from gravity and geodynamic modelling. *Tectonophysics*, *766*, 453–468. https://doi.org/10.1016/j.tecto.2019.06.025

Insel, N., Grove, M., Haschke, M., Barnes, J. B., Schmitt, A. K., & Strecker, M. R. (2012). Paleozoic to early Cenozoic cooling and exhumation of the basement underlying the eastern Puna Plateau margin prior to plateau growth. *Tectonics*, *31*(6), TC6006. https://doi.org/10.1029/2012tc003168

Jackson, J. A., Austrheim, H., McKenzie, D., & Priestley, K. (2004). Metastability, mechanical strength, and the support of mountain belts. *Geology*, *32*(7), 625–628. https://doi.org/10.1130/g20397.1

Jordan, T. E., & Allmendinger, R. W. (1986). The Sierras Pampeanas of Argentina; a modern analogue of Rocky Mountain foreland deformation. *American Journal of Science*, *286*(10), 737–764. https://doi.org/10.2475/ajs.286.10.737

Jordan, T. E., Isacks, B. L., Allmendinger, R. W., Brewer, J. A., Ramos, V. A., & Ando, C. J. (1983). Andean tectonics related to geometry of subducted Nazca plate. *GSA Bulletin*, *94*(3), 341–361. https://doi.org/10.1130/0016-7606(1983)94<341:atrtgo>2.0.co;2

Kay, S. M., Mpodozis, C., & Coira, B. (1999). Neogene magmatism, tectonism, and mineral deposits of the Central Andes (22° to 33°S latitude). In B. J. Spencer (Ed.), *Geology and ore deposits of the Central Andes, Special Publication* (pp. 27–59). Society of Economic Geology. https://doi.org/10.5382/sp.07.02

Kay, S. M., Ramos, V. A., Dickinson, W. R., & Coira, B. L. (2009). *Backbone of the Americas: Shallow subduction, plateau uplift, and ridge and terrane collision*. Geological Society of America. https://doi.org/10.1130/2009.1204(11)

Ketcham, R. A. (2005). The role of crystallographic angle in characterizing and modeling apatite fission-track length data. *Radiation Measurements*, *39*(6), 595–601. https://doi.org/10.1016/j.radmeas.2004.07.008

Ketcham, R. A., Donelick, R. A., & Carlson, W. D. (1999). Variability of apatite fission-track annealing kinetics: III. Extrapolation to geological time scales. *American Mineralogist*, *84*(9), 1235–1255. https://doi.org/10.2138/am-1999-0903

Kley, J., & Monaldi, C. R. (2002). Tectonic inversion in the Santa Barbara System of the central Andean foreland thrust belt, northwestern Argentina. *Tectonics*, *21*(6), 1061. https://doi.org/10.1029/2002tc902003

Kley, J., Rossello, E. A., Monaldi, C. R., & Habighorst, B. (2005). Seismic and field evidence for selective inversion of Cretaceous normal faults, Salta rift, northwest Argentina. *Tectonophysics*, *399*(1–4), 155–172. https://doi.org/10.1016/j.tecto.2004.12.020

Kraemer, B., Adelmann, D., Alten, M., Schnurr, W., Erpenstein, K., Kiefer, E., et al. (1999). Incorporation of the Paleogene foreland into the Neogene Puna Plateau: The Salar de Antofalla area, NW Argentina. *Journal of South American Earth Sciences*, *12*(2), 157–182. https://doi.org/10.1016/s0895-9811(99)00012-7

Lamb, S., & Hoke, L. (1997). Origin of the high plateau in the Central Andes, Bolivia, South America. *Tectonics*, *16*(4), 623–649. https://doi.org/10.1029/97tc00495

Lapiana, A. T. (2021). *Evolución de los sistemas fluviales en la region de antepaís Paleocena – Neógena en la region de Sierra Aguilar – Tres Cruces, Noreste Argentino* (PhD thesis). Universidad de Cordoba.

Löbens, S., Sobel, E. R., Bense, F. A., Wemmer, K., Dunkl, I., & Siegesmund, S. (2013). Refined exhumation history of the northern Sierras Pampeanas, Argentina. *Tectonics*, *32*(3), 453–472. https://doi.org/10.1002/tect.20038

López Steinmetz, R. L., & Galli, C. I. (2015). Basin development at the eastern border of the Northern Puna and its relationship with the plateau evolution. *Journal of South American Earth Sciences*, *63*, 244–259. https://doi.org/10.1016/j.jsames.2015.07.017

López Steinmetz, R. L., & Montero-López, C. (2019). Stratigraphy and sedimentary environments of the Villa María and Peña Colorada formations (Paleogene), westernmost Argentine Plateau. *Latin American Journal of Sedimentology and Basin Analysis*, *26*, 39–56.

Maksaev, V. (1990). *Metallogeny, geological evolution, and thermochronology of the Chilean Andes between latitudes 21° and 26° south, and the origin of major porphyry copper deposits* (PhD thesis). Dalhousie University.

Maksaev, V., & Zentilli, M. (1999). Fission track thermochronology of the Domeyko Cordillera, northern Chile: Implications for Andean tectonics and porphyry copper metallogenesis. *Exploration And Mining Geology*, *8*, 65–90.

Marquillas, R. A., del Papa, C., & Sabino, I. F. (2005). Sedimentary aspects and paleoenvironmental evolution of a rift basin: Salta Group (Cretaceous–Paleogene), northwestern Argentina. *International Journal of Earth Sciences*, *94*(1), 94–113. https://doi.org/10.1007/s00531-004-0443-2

Marquillas, R. A., & Salfity, J. A. (1988). Tectonic framework and correlations of the cretaceous-ecocene salta group; Argentina. In *The southern Central Andes* (pp. 119–136). Springer.

Marshak, S., Karlstrom, K., & Timmons, J. M. (2000). Inversion of Proterozoic extensional faults: An explanation for the pattern of Laramide and Ancestral Rockies intracratonic deformation, United States. *Geology*, *28*(8), 735–738. https://doi.org/10.1130/0091-7613(2000)28<735:iopefa>2.0.co;2

Martínez, F., Muñoz, B., López, C., González, R., Parra, M., & Riquelme, R. (2021). Complex basement-involved contractional structures in the Pre-Andean basins of northern Chile: A review from seismic data. *Tectonics*, *40*(2), e2020TC006433. https://doi.org/10.1029/2020tc006433

McQuarrie, N. (2002). The kinematic history of the central Andean fold-thrust belt, Bolivia: Implications for building a high plateau. *GSA Bulletin*, *114*(8), 950–963. https://doi.org/10.1130/0016-7606(2002)114<0950:tkhotc>2.0.co;2

McQuarrie, N., Horton, B. K., Zandt, G., Beck, S., & DeCelles, P. G. (2005). Lithospheric evolution of the Andean fold–thrust belt, Bolivia, and the origin of the central Andean Plateau. *Tectonophysics*, *399*(1–4), 15–37. https://doi.org/10.1016/j.tecto.2004.12.013

Méndez, V., Navarini, A., Plaza, D., & Viera, V. (1973). Faja Eruptiva de la Puna Oriental. In *Actas del 5th Congreso Geológico Argentino* (Vol. 4, pp. 89–100). Asociación Geológica Argentina.

Mon, R., & Salfity, J. A. (1995). Tectonic evolution of the Andes of northern Argentina. In A. J. Tankard, R. Suarez-Soruco, & H. J. Welsink (Eds.), *Petroleum basins of South America*, *AAPG Memoirs* (Vol. 62, pp. 269–283). https://doi.org/10.1306/m62593c12

Montero-López, C., Ballato, P., & Aramayo, A. (2017). *New evidences of the Paleogene and Early Miocene unconformity in the Quebrada de Carachi, El Toro basin, Cordillera Oriental (NW Argentina)*. Paper presented at XX Congreso Geológico Argentino, San Miguel de Tucumán, Argentina.

Montero-López, C., del Papa, C., Hongn, F., Strecker, M. R., & Aramayo, A. (2018). Synsedimentary broken-foreland tectonics during the Paleogene in the Andes of NW Argentine: New evidence from regional to centimetre-scale deformation features. *Basin Research*, *30*, 142–159. https://doi.org/10.1111/bre.12212

Montero-López, C., Hongn, F., López Steinmetz, R. L., Aramayo, A., Pingel, H., Strecker, M. R., et al. (2021). Development of an incipient Paleogene topography between the present-day Eastern Andean Plateau (Puna) and the Eastern Cordillera, southern Central Andes, NW Argentina. *Basin Research*, *33*(2), 1194–1217. https://doi.org/10.1111/bre.12510

Mora, A., Parra, M., Strecker, M. R., Kammer, A., Dimaté, C., & Rodríguez, F. (2006). Cenozoic contractional reactivation of Mesozoic extensional structures in the Eastern Cordillera of Colombia. *Tectonics*, *25*(2), TC2010. https://doi.org/10.1029/2005tc001854

Mortimer, E., Carrapa, B., Coutand, I., Schoenbohm, L., Sobel, E. R., Gomez, J. S., & Strecker, M. R. (2007). Fragmentation of a foreland basin in response to out-of-sequence basement uplifts and structural reactivation: El Cajón–Campo del Arenal basin, NW Argentina. *GSA Bulletin*, *119*(5–6), 637–653. https://doi.org/10.1130/b25884.1

Mpodozis, C., Arriagada, C., Basso, M., Roperch, P., Cobbold, P., & Reich, M. (2005). Late Mesozoic to Paleogene stratigraphy of the Salar de Atacama Basin, Antofagasta, Northern Chile: Implications for the tectonic evolution of the Central Andes. *Tectonophysics*, *399*(1–4), 125–154. https://doi.org/10.1016/j.tecto.2004.12.019

Omarini, R. H., Sureda, R. J., Götze, H.-J., Seilacher, A., & Pflüger, F. (1999). Puncoviscana folded belt in northwestern Argentina: Testimony of Late Proterozoic Rodinia fragmentation and pre-Gondwana collisional episodes. *International Journal of Earth Sciences*, *88*(1), 76–97. https://doi.org/10.1007/s005310050247

Oncken, O., Hindle, D., Kley, J., Elger, K., Victor, P., & Schemmann, K. (2006). Deformation of the central Andean upper plate system – Facts, fiction, and constraints for plateau models. In O. Oncken, G. Chong, G. Franz, P. Giese, H.-J. Götze, V. A. Ramos, et al. (Eds.), *The Andes, active subduction orogeny, Frontiers in Earth Science* (pp. 3–27). Springer-Verlag Berlin Heidelberg. https://doi.org/10.1007/978-3-540-48684-8_1

Parra, M., Mora, A., Sobel, E. R., Strecker, M. R., & González, R. (2009). Episodic orogenic front migration in the northern Andes: Constraints from low-temperature thermochronology in the Eastern Cordillera, Colombia. *Tectonics*, *28*(4), TC4004. https://doi.org/10.1029/2008tc002423

Paton, C., Woodhead, J. D., Hellstrom, J. C., Hergt, J. M., Greig, A., & Maas, R. (2010). Improved laser ablation U-Pb zircon geochronology through robust downhole fractionation correction. *Geochemistry, Geophysics, Geosystems*, *11*(3), Q0AA06. https://doi.org/10.1029/2009gc002618

Payrola, P., del Papa, C., Aramayo, A., Pingel, H., Hongn, F., Sobel, E. R., et al. (2020). Episodic out-of-sequence deformation promoted by Cenozoic fault reactivation in NW Argentina. *Tectonophysics*, *776*, 228276. https://doi.org/10.1016/j.tecto.2019.228276

Payrola, P., Powell, J., del Papa, C., & Hongn, F. (2009). Middle Eocene deformation–sedimentation in the Luracatao Valley: Tracking the beginning of the foreland basin of northwestern Argentina. *Journal of South American Earth Sciences*, *28*(2), 142–154. https://doi.org/10.1016/j.jsames.2009.06.002

Payrola, P., Zapata, S., Sobel, E. R., del Papa, C., Pingel, H., Glodny, J., & Ledesma, J. (2021). Exhumation and structural evolution of the high-elevation Malcante range, Eastern Cordillera, NW Argentina. *Journal of South American Earth Sciences*, *105*, 102990. https://doi.org/10.1016/j.jsames.2020.102990

Pearson, D. M., Kapp, P., DeCelles, P. G., Reiners, P. W., Gehrels, G. E., Ducea, M. N., & Pullen, A. (2013). Influence of pre-Andean crustal structure on Cenozoic thrust belt kinematics and shortening magnitude: Northwestern Argentina. *Geosphere*, *9*(6), 1766–1782. https://doi.org/10.1130/ges00923.1

Pearson, D. M., Kapp, P., Reiners, P. W., Gehrels, G. E., Ducea, M. N., Pullen, A., et al. (2012). Major Miocene exhumation by fault-propagation folding within a metamorphosed, early Paleozoic thrust belt: Northwestern Argentina. *Tectonics*, *31*(4), TC4023. https://doi.org/10.1029/2011tc003043

Pingel, H., Alonso, R. N., Altenberger, U., Cottle, J., & Strecker, M. R. (2019). Miocene to Quaternary basin evolution at the southeastern Andean Plateau (Puna) margin (ca. 24°S lat, Northwestern Argentina). *Basin Research*, *31*(4), 808–826. https://doi.org/10.1111/bre.12346

Pingel, H., Alonso, R. N., Mulch, A., Rohrmann, A., Sudo, M., & Strecker, M. R. (2014). Pliocene orographic barrier uplift in the southern Central Andes. *Geology*, *42*(8), 691–694. https://doi.org/10.1130/g35538.1

Pingel, H., Strecker, M. R., Alonso, R. N., & Schmitt, A. K. (2013). Neotectonic basin and landscape evolution in the Eastern Cordillera of NW Argentina, Humahuaca Basin (~24°S). *Basin Research*, *25*(5), 554–573. https://doi.org/10.1111/bre.12016

Pingel, H., Strecker, M. R., Mulch, A., Alonso, R. N., Cottle, J., & Rohrmann, A. (2020). Late Cenozoic topographic evolution of the Eastern Cordillera and Puna Plateau margin in the southern Central Andes (NW Argentina). *Earth and Planetary Science Letters*, *535*, 116112. https://doi.org/10.1016/j.epsl.2020.116112

Popov, D. V., & Spikings, R. A. (2020). Diffusion vs. fluid alteration in alkali feldspar ^{40}Ar/^{39}Ar thermochronology: Does cross-correlation of log(r/r0) and age spectra validate thermal histories? *Chemical Geology*, *539*, 119506. https://doi.org/10.1016/j.chemgeo.2020.119506

Rahl, J. M., Harbor, D. J., Galli, C. I., & O'Sullivan, P. (2018). Foreland Basin record of uplift and exhumation of the Eastern Cordillera, Northwest Argentina. *Tectonics*, *37*(11), 4173–4193. https://doi.org/10.1029/2017tc004955

Ramos, V. A. (1999). Plate tectonic setting of the Andean Cordillera. *Episodes*, *22*(3), 183–190. https://doi.org/10.18814/epiiugs/1999/v22i3/005

Ramos, V. A., & Folguera, A. (2009). Andean flat-slab subduction through time. *Geological Soc Lond Special Pub*l, *327*(1), 31–54. https://doi.org/10.1144/sp327.3

Reiners, P. W., Thomson, S. N., Vernon, A., Willett, D., Zattin, M., Einhorn, J., et al. (2015). Low-temperature thermochronologic trends across the Central Andes, 21°S–28°S. In P. G. DeCelles, M. N. Ducea, B. Carrapa, & P. A. Kapp (Eds.), *Geodynamics of a Cordilleran orogenic system: The Central Andes of Argentina and northern Chile*. Geological Society of America. https://doi.org/10.1130/2015.1212(12)

Reynolds, J. H., Galli, C. I., Hernández, R. M., Idleman, B. D., Kotila, J. M., Hilliard, R. V., & Naeser, C. W. (2000). Middle Miocene tectonic development of the transition zone, Salta Province, northwest Argentina: Magnetic stratigraphy from the Metán Subgroup, Sierra de González. *GSA Bulletin*, *112*(11), 1736–1751. https://doi.org/10.1130/0016-7606(2000)112<1736:mmtdot>2.0.co;2

Riller, U., Cruden, A. R., Boutelier, D., & Schrank, C. E. (2012). The causes of sinuous crustal-scale deformation patterns in hot orogens: Evidence from scaled analogue experiments and the southern Central Andes. *Journal of Structural Geology*, *37*, 65–74. https://doi.org/10.1016/j.jsg.2012.02.002

Salfity, J. A., & Marquillas, R. A. (1994). Tectonic and sedimentary evolution of the Cretaceous-Eocene Salta Group basin, Argentina. In J. A. Salfity (Ed.), *Cretaceous tectonics of the Andes* (pp. 266–315). Earth Evolution Sciences. https://doi.org/10.1007/978-3-322-85472-8_6

Schwab, K. (1973). Die Stratigraphie in der Umgebung des Salar de Cauchari (NW-Argentinien): E. Beitrag zur erdgeschichtlichen Entwicklung der Puna. In *Geotektonische Forschungen* (Vol. 43). Schweizerbart.

Schwab, K., & Lippolt, H. (1976). K-Ar mineral ages and Late Cenozoic history of the Salar de Cauchari area (Argentine Puna). In O. Gonzalez-Ferran (Ed.), *Proceedings of the Symposium of Andean and Antarctic Volcanology Problems, Santiago de Chile, Chile, September 1974* (pp. 698–714). IAVCEI - International Association of Volcanology and Chemistry of the Earth's Interior.

Seggiaro, R. E. (1994). *Petrología, geoquímica y mecanismos de erupción del complejo volcánico Coranzulí* (PhD thesis). Universidad Nacional de Salta.

Seggiaro, R. E., Becchio, R., Bercheñi, V., Ramallo, L., & Franchi, M. (2015). *Hoja Geológica 2366-III Susques, Provincias de Jujuy y Salta* (Boletín, 414, p. 103). Instituto de Geología y Recursos Minerales, Servicio Geológico Minero Argentino.

Seggiaro, R. E., Guzmán, S. R., & Martí, J. (2019). Dynamics of caldera collapse during the Coranzulí eruption (6.6 Ma) (Central Andes, Argentina). *Journal of Volcanology and Geothermal Research*, *374*, 1–12. https://doi.org/10.1016/j.jvolgeores.2019.02.003

Siks, B. C., & Horton, B. K. (2011). Growth and fragmentation of the Andean foreland basin during eastward advance of fold-thrust deformation, Puna Plateau and Eastern Cordillera, northern Argentina. *Tectonics*, *30*(6), TC6017. https://doi.org/10.1029/2011tc002944

Sobel, E. R., & Dumitru, T. A. (1997). Thrusting and exhumation around the margins of the western Tarim basin during the India-Asia collision. *Journal of Geophysical Research*, *102*(B3), 5043–5063. https://doi.org/10.1029/96jb03267

Sobel, E. R., Hilley, G. E., & Strecker, M. R. (2003). Formation of internally drained contractional basins by aridity-limited bedrock incision. *Journal of Geophysical Research*, *108*(B7), 2344. https://doi.org/10.1029/2002jb001883

Sobel, E. R., & Seward, D. (2010). Influence of etching conditions on apatite fission-track etch pit diameter. *Chemical Geology*, *271*(1–2), 59–69. https://doi.org/10.1016/j.chemgeo.2009.12.012

Sobel, E. R., & Strecker, M. R. (2003). Uplift, exhumation and precipitation: Tectonic and climatic control of Late Cenozoic landscape evolution in the northern Sierras Pampeanas, Argentina. *Basin Research*, *15*(4), 431–451. https://doi.org/10.1046/j.1365-2117.2003.00214.x

Stalder, N. F., Herman, F., Fellin, M. G., Coutand, I., Aguilar, G., Reiners, P. W., & Fox, M. (2020). The relationships between tectonics, climate and exhumation in the Central Andes (18–36°S): Evidence from low-temperature thermochronology. *Earth-Science Reviews*, *210*, 103276. https://doi.org/10.1016/j.earscirev.2020.103276

Strecker, M. R., Alonso, R., Bookhagen, B., Carrapa, B., Coutand, I., Hain, M. P., et al. (2009). Does the topographic distribution of the central Andean Puna Plateau result from climatic or geodynamic processes? *Geology*, *37*(7), 643–646. https://doi.org/10.1130/g25545a.1

Strecker, M. R., Alonso, R. N., Bookhagen, B., Carrapa, B., Hilley, G. E., Sobel, E. R., & Trauth, M. H. (2007). Tectonics and climate of the southern Central Andes. *Annual Review of Earth and Planetary Sciences*, *35*(1), 747–787. https://doi.org/10.1146/annurev.earth.35.031306.140158

Strecker, M. R., Cerveny, P., Bloom, A. L., & Malizia, D. (1989). Late Cenozoic tectonism and landscape development in the foreland of the Andes: Northern Sierras Pampeanas (26°–28°S), Argentina. *Tectonics*, *8*(3), 517–534. https://doi.org/10.1029/tc008i003p00517

Strecker, M. R., Hilley, G. E., Bookhagen, B., & Sobel, E. R. (2012). Structural, geomorphic, and depositional characteristics of contiguous and broken foreland basins: Examples from the eastern flanks of the Central Andes in Bolivia and NW Argentina. In C. Busby & A. Azor (Eds.), *Tectonics of sedimentary basins: Recent advances* (pp. 508–521). Blackwell Publishing. https://doi.org/10.1002/9781444347166.ch25

Talling, P. J., Lawton, T. F., Burbank, D. W., & Hobbs, R. S. (1995). Evolution of latest Cretaceous–Eocene nonmarine deposystems in the Axhandle piggyback basin of central Utah. *GSA Bulletin*, *107*, 297–315. https://doi.org/10.1130/0016-7606(1995)107<0297:eolcen>2.3.co;2

Tapponnier, P., Meyer, B., Avouac, J. P., Peltzer, G., Gaudemer, Y., Shunmin, G., et al. (1990). Active thrusting and folding in the Qilian Shan, and decoupling between upper crust and mantle in northeastern Tibet. *Earth and Planetary Science Letters*, *97*(3–4), 382–403. https://doi.org/10.1016/0012-821x(90)90053-z

Vermeesch, P. (2018). IsoplotR: A free and open toolbox for geochronology. *Geoscience Frontiers*, *9*(5), 1479–1493. https://doi.org/10.1016/j.gsf.2018.04.001

Vezzoli, L., Acocella, V., Omarini, R., & Mazzuoli, R. (2012). Miocene sedimentation, volcanism and deformation in the Eastern Cordillera (24°30′ S, NW Argentina): Tracking the evolution of the foreland basin of the Central Andes. *Basin Research*, *24*(6), 637–663. https://doi.org/10.1111/j.1365-2117.2012.00547.x

Wiedenbeck, M., Allé, P., Corfu, F., Griffin, W. L., Meier, M., Oberli, F., et al. (1995). Three natural zircon standards for U-Th-Pb, Lu-Hf, trace element and REE analyses. *Geostandards Newsletter*, *19*, 1–23. https://doi.org/10.1111/j.1751-908x.1995.tb00147.x

Wolfe, M. R., & Stockli, D. F. (2010). Zircon (U–Th)/He thermochronometry in the KTB drill hole, Germany, and its implications for bulk He diffusion kinetics in zircon. *Earth and Planetary Science Letters*, *295*(1–2), 69–82. https://doi.org/10.1016/j.epsl.2010.03.025

Zapata, S., Sobel, E. R., del Papa, C., & Glodny, J. (2020). Upper Plate Controls on the formation of broken foreland basins in the Andean retroarc between 26°S and 28°S: From Cretaceous rifting to Paleogene and Miocene broken foreland basins. *Geochemistry, Geophysics, Geosystems*, *21*(7), e2019GC008876. https://doi.org/10.1029/2019gc008876

Zhou, R., Schoenbohm, L. M., Sobel, E. R., Davis, D. W., & Glodny, J. (2017). New constraints on orogenic models of the southern Central Andean Plateau: Cenozoic basin evolution and bedrock exhumation. *GSA Bulletin*, *129*(1–2), 152–170. https://doi.org/10.1130/b31384.1